A performance study to the spatial and energy resolution of a hybrid pixel detector for alpha imaging applications

by

J.W.J. Hoefsloot

to obtain the degree of Master of Science
at the Delft University of Technology

Student number:	4380614	
Project duration:	April 24, 2021 – January 28, 2022	
Thesis committee:	Dr. ir. A. G. Denkova,	TU Delft, supervisor
	Dr. ir. M. C. Goorden,	TU Delft
	Dr. ir. R. de Kruijff,	TU Delft

An electronic version of this thesis is available at `http://repository.tudelft.nl/`.

Acknowledgements

I would like to thank all my colleagues from Applied Radiation Isotopes (ARI), who provided me with insights and expertise that greatly assisted the research. I would like to thank the SBD for their cooperation and patience with me. I would like to thank Dr. ir. A. G. Denkova for the supervision of this project and for the opportunity to work on this project. But foremost I would like to thank Dr. ing. J. Plomp for the daily supervision, his assistance in performing and analyzing measurement and the day-to-day talks that we had.

Abstract

Targeted Alpha Therapy (TAT) is an interesting technique in tumour treatments, especially in the treatment of local tumours or the treatments of solid tumours while minimizing unwanted radiation to surrounding tissue. The use of Ac-225 in TAT is especially interesting as in the decay of Ac-225 four alpha particles are emitted. The recoil effect will however disrupt the daughter nuclide from the targetting molecule, allowing the daughter nuclide to drift away from the tumour cells to healthy tissue. In order to study the redistribution of radionuclides due to the recoil effect imaging tools are required. An existing technique is the classic alpha camera, this technique is based on the scintillation of alpha particles. Emitted photons by the scintillating layer are registered by a charge coupled device. This technique allows for a spatial resolution of up to 35 μm but is limited by the uptake of other radiation forms (photon, beta).

Another alpha imaging technique is called the Timepix, this is a hybrid pixelated semiconducting sensor that consists of an array of 55 μm square pixels. The semiconducting material (silicon) converts ionizing radiation into charge carriers that are collected at pixel sites. In this research the limitations of the Timepix chip with regard to spatial & energy resolution in alpha particle imaging are investigated.

The spatial resolution was investigated by the use of fine edged alpha absorbing objects, a small pitched collimators to ensure a monochromatic beam of alpha particles, and an alpha emitting source (Am-241). The Timepix chip registered the incoming alpha particles. By binning the counted alpha particles in small intervals a step function was obtained, from which a Gaussian function was obtained. The Full Width at Halve Maximum (FWHM) is a measure of (spatial) resolution of the Gaussian function. Results showed a spatial resolution of 9.8 μm obtained by a collimator with pitch of 6 μm. The obtained spatial resolution shows that sub-pixel resolution in alpha particle imaging is possible.

The energy resolution of the Timepix chip was investigated by the use of a collimator to ensure a monochromatic beam of alpha particles, several Mylar foils to slow down the alpha particles and an alpha emitting source (Am-241). The use of the time over threshold mode (TOT) indicates the amount of time a signal is above threshold, which is a direct indication of the particles energy. Output of the chip is Gaussian shaped, from which the energy resolution was obtained. The obtained energy resolution of the Timepix chip was 0.8 MeV, which allows for identification of most daughter nuclides from the decay chain of Ac-225. This energy resolution does not allow for the identification of the disintegration of Fr-221 (6.64 MeV) and Ac-225 (5.94 MeV).

Contents

1

Introduction

In 1775 Percival Pott identified a causal relationship between the exposure to chimney soot and the likelihood of cell carcinoma of the scrotum amongst chimney sweepers [1]. In his report, Pott is the first to link environmental exposure to the development of cancer. His discovery was the first milestone in cancer research & discovery. Present technology tells us much more about cancer and how to battle it, but in modern times cancer is still one of the leading causes of deaths world wide. In 2020 cancer caused over 10 million deaths [2]. Common cancer treatments involve surgery, chemotherapy, and radiotherapy. Radiotherapy is a treatment of cancer that uses high doses of radiation to eliminate cancer cells and shrink tumours. There are three types of radiotherapy: external beam, brachytherapy (radioactive source is temporary being placed near tumour), and radionuclide therapy.

Radionuclide therapy uses radio-isotopes that are targeted to tumours by tumour selective molecules. Ionizing radiation which is often used in radionuclide therapy are beta (electron) and alpha-radiation. Compared to beta radiation, alpha-emitting radionuclides emit alpha's with a high Linear Energy Transfer (LET) and the emitted alpha's are short ranged. The high LET and short range of ionizing particles makes sure that all energy is deposited in a small range, thus minimizing the radiobiological damage to surrounding, healthy tissue as long as the targeting of alpha-emitting radionuclides to tumour cells is successful. The main interest for targeted alpha therapy (TAT) lies in the treatment of local tumours, and the treatment of solid tumours while minimizing unwanted radiation to surrounding tissue [3]. In 2013 the first clinical TAT applications with Ra-223 dichloride were approved by the U.S. Food and Drug Administration (FDA) and is used in the therapy for bone metastases in castration-resistant prostate cancer [4].

The growing interest in TAT as an efficient tool in tumour therapies can be partially explained by the success of the clinical applications of Ra-223 dichloride in bone metastases. Besides Ra-223, there are several other radionuclides of interest for TAT. Ac-225 is such a radionuclide: just as Ra-223, Ac-225 decays via several alpha's and beta's. A multi-emitting alpha radionuclide is of great interest for TAT as per delivered radionuclide, multiple alpha's can be delivered to tumour material. However, a multi-emitting radionuclide does have to cope with the recoil effect. Energy that is released in the disintegration of the parent radionuclide is distributed over the ionizing particle and the daughter nuclide. Because of this effect the daughter nuclide will disrupt from the targetting molecule [5]. This effect is undesirable as the daughter nuclide can drift away from the tumour site to healthy tissue.

In order to study the redistribution of radionuclides due to the recoil effect tools are required to provide knowledge on activity and energy distribution of the redistribution of the targeted daughter radionuclides. Imaging alpha radiation in biological samples is not that easy. In order to image the short ranged alpha's, several μm in tissue [6], one would need to have ex-vivo biological alpha-treated sample in order to be able to image the short-ranged alpha's. There are two described methods to image alpha particles in biological samples:

1.1. The classic alpha-camera

The classic alpha-camera, introduced by Bäck and Jacobsson from the Swedish University of Gothenburg is quantitative imaging technique that can detect alpha-particles ex-vivo [7]. The techniques makes use of a scintillating material that emits photons when upon alpha particles hit the scintillating material. A charge-coupled device (CCD) registers the emitted photons. Results showed a total spatial resolution of up to $35\mu m$. A schematic view of the technique is given in figure 1.1.

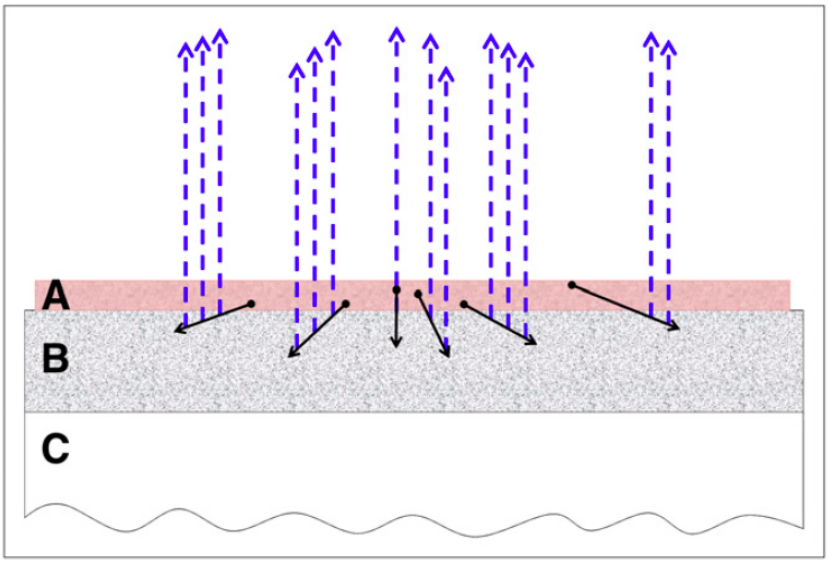

Figure 1.1: The classic alpha camera, the device consists of three layers: Alpha's are emitted from cryosections of alpha-treated mice (A), and are placed on a scintillating layer (B) which was coated on a clear polyester sheet (C). Image retrieved from [7].

The classic alpha-camera is a great tool for ex vivo detection and activity distribution assessment of alpha particles in tissue on a sub-organ level. A problem for this technique is that the scintillating layer does not only absorb alpha's but also possibly absorbs other radiation types such as photons (gamma and x-ray) and beta radiation emitted from radioactive decay. This limits the study to individual alpha particles as alpha particles can not be distinguished from absorbed photons.

1.2. Chip Based Radiation Detection

An alternative technique of imaging ex-vivo alpha radiation is a hybrid pixel imaging detector called the Medipix family. This is a technique developed by physicist of CERN which has already evolved to several devices like the Medipix2 and Timepix. All devices are based on the same technique: radiation is detected based on direct conversion of radiation into charge in a sensitive layer. This sensitive layer is a semiconducting material (silicon), when radiation is absorbed in silicon the radiation is converted into charge which is collected at pixel bonds [8, 9]. The device consists of single arrays of square ordered pixels, each pixel contains an individual integrated signal processing circuit such that pixels can be operated and examined individually. The Timepix is the successor of the Medipix2 chip. The chips are much alike, but the electronics of the Timepix chip is more advanced. The main difference lies in the operating modes of the chips, the Timepix can be operated in three modes: Medipix mode (counting mode), time over threshold (TOT), and time of arrival (TOA). TOT and TOA mode can be used for identification of particle incidence (TOA) and particle energy (TOT) [10].

1.3. Research Goal

Timepix has already demonstrated that it has relevant applications in autoradiography imaging in TAT [11, 12]. The question however, lies in the limitations of the Timepix chip. In order to study recoil effects and to gain more knowledge of damage of TAT to healthy tissue an imaging system with a resolution of several μm is required. Moreover, it is desirable to identify daughter atoms in the decay chain of heavy elements (f.e. Ac-225, or Ra-223). The emitted alpha particles differ in decay energy, thus the Timepix TOT mode could provide information on these emitted particles. The four alpha particles emitted in the most common decay route of Ac-225 are via: Ac-225 –> Fr-221 + 5.94 MeV alpha –> At-217 + 6.46 MeV alpha –> Bi-213 + 7.20 MeV alpha. Bi-213 most often (97%) decays to Po-213 via beta decay. Then in the decay to Pb-209 another alpha of 8.54 MeV is emitted. Part of this research focus will lie in the determination of the Timepix energy resolution such that we can identify the type of disintegration in the decay chain of Ac-225. The goal of this thesis is to identify the limitations of the Timepix chip regarding alpha particle imaging. To obtain this goal in this thesis two research questions have been set up:

- What is the spatial resolution of the Timepix chip regarding alpha particle imaging?
- Is it possible to identify the daughter radionuclides Fr-221, At-217, Bi-213 and Pb-209 based on the energy of its alpha decay captured on a Timepix chip and what is the energy resolution of the chip regarding alpha particle imaging?

2

Theory

2.1. Ionizing Radiation

Ionizing radiation is radiation with enough energy to remove bounded electrons from the orbit of atoms, with the effect that the atom will become ionized or positively charged. Ionizing radiation can be encountered in two ways, either as an electromagnetic wave (gamma & x-ray) or as a particle (beta & alpha). Ionizing radiation is the result of the spontaneous disintegration of unstable atoms (radionuclides), whilst disintegration other less heavy atoms are formed together with a form of excess energy (ionizing radiation). The radioactive decay can be seen as:

$$A \rightarrow \sum_i B_i + Q \tag{2.1}$$

In which A is the radionuclide, B_i are the formed atoms (with mass of A $\geq$ mass of $\sum_i B_i$) and Q is the emitted radiation (energy).

2.1.1. Ionizing Electromagnetic Waves

Electromagnetic (EM) radiation is radiation emitted on the whole EM spectrum and thus is a photon. Depending on the wavelength the energy is described by:

$$E = hf = \frac{hc}{\lambda} \tag{2.2}$$

In this equation h is the constant of Planck, f is the frequency of the photon, c is the speed of light in vacuum and λ is the wavelength of the photon.

Radiation on the EM spectrum is only ionizing radiation when the emitted photon has enough energy to ionize an atom or molecule, for example it takes a 13.6 eV photon to ionize a hydrogen atom. In radiodiagnostics low energy x-rays are used for imaging and in radiotherapy high energy x-rays and gamma's are used for tumour treatment.

The production of x-rays and gamma's is not alike, x-rays are produced due to electronic interactions. This can either be due to the rearrangement of (excited) electrons in atoms or x-rays can also be produced when electrons strike a metal target. Gamma radiation is formed when a parent nucleus is in an excited state and needs to lose its energy thus emitting a gamma. When this excited nucleus exists for quite some time we speak of a metastable state. A common gamma emitter used in medical services is Technicium-99m and its decay mode is give by:

$$^{99m}_{43}Tc \rightarrow ^{99}_{43}Tc + \gamma \tag{2.3}$$

2.1.2. Particle-like Ionizing Radiation

As mentioned there is another form of ionizing radiation next to electromagnetic ionizing radiation: particle like ionizing radiation. Typical decay modes include alpha or beta decay.

Eq. 2.1 shows a basic decay mode, these decay modes are limited by conservation of total atomic number and total mass number of the decay. For an atom B, represented in eq. 2.4 'Z' is the total number of protons in an atom and 'A' is the total number of protons plus neutrons in an atom.

$$^{A}_{Z}B \tag{2.4}$$

Alpha decay is type of decay where besides a daughter atom a $^{4}_{2}He$ atom is produced. Typical (kinetic) energies of the produced alpha are of several MeV's.

Beta decay is type of decay where besides a daughter atom an electron ($^{0}_{-1}\beta$) or positron ($^{0}_{1}\beta$) is formed plus an antineutrino or neutrino. The energy of an emitted beta particle is described by a distribution function as energy released in the decay is distributed over the (anti)neutrino and beta-particle. The energy of a beta particles thus is described by a spectrum ranging from 0 to several MeV's.

2.1.3. Radiation Quality & Attenuation

In assessing the type of radiation to use for biomedical purposes one takes the possible effects of harm due to ionizing radiation into account. The absorbed dose is a quantity which is a measure for the energy deposited by ionizing radiation per unit mass and its SI unit is Grey (G = J/kg). The effective dose is a dose quantity which both weighted for tissue sensitivity and radiation quality. For example an alpha does 20 times more damage than a gamma. The quality factor for a gamma and beta is 1, and thus for an alpha is 20 [13]. Alpha radiation is thus the most potent form of ionizing radiation for biological samples, but shielding alpha radiation is rather easy. When emitted alpha particles have high kinetic energy (several MeV's) but alpha particles also are massive, as they are Helium ions. Because of its high mass alpha radiation is easy to shield, one would only need a piece of paper. The total path length of alpha particles in air is just a few centimeters, the range of a 5.49 MeV alpha is 4.2 centimeter [14].

Beta radiation (β^-, β^+) has much lower mass compared to alpha's ($m_{He^{2+}}$ / m_e ~ 8000) as beta-minus and beta-plus are electrons and positrons respectively. The range of a beta particle is just as an alpha energy dependent. Common energies of beta particles are in the range between few KeV to several MeV. Strontium-90, a common used beta-minus emitting radioisotope, has a decay energy of 0.55 MeV. For this beta particle the range in air is over 1 meter, therefore more intensive shielding is necessary. Plastic is a common used material to shield beta radiation, the range for a 0.55 MeV beta in polyethylene (plastic) is 0.2 centimeters [15].

Gamma (or x-ray) radiation is more difficult to shield, most used shielding technique of electromagnetic radiation includes lead plates.

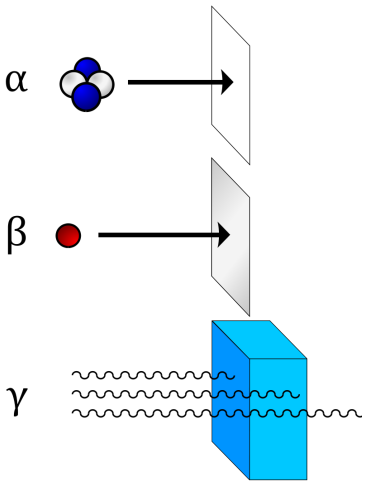

Figure 2.1: Shielding radiation. Alpha radiation is rather massive w.r.t. beta and gamma, and thus is shielded more easy. A piece of paper will not surpass alpha radiation, a plastic sheet will shield all beta radiation. Gamma's are more difficult as a few centimeters of lead is needed to shield high energy gamma's. Image retrieved from [16].

2.2. Alpha Particles as a Killing Agent

Typically the range of alpha radiation in tissue is 50-100 μm, which is about the size of a few cells in the human body [17]. Over this small distance all incidental kinetic energy of the alpha particle is transferred to its surroundings and thus stopping the alpha particle. The energy transfer of an alpha particle can be represented by the Bragg curve, given in figure 2.2.

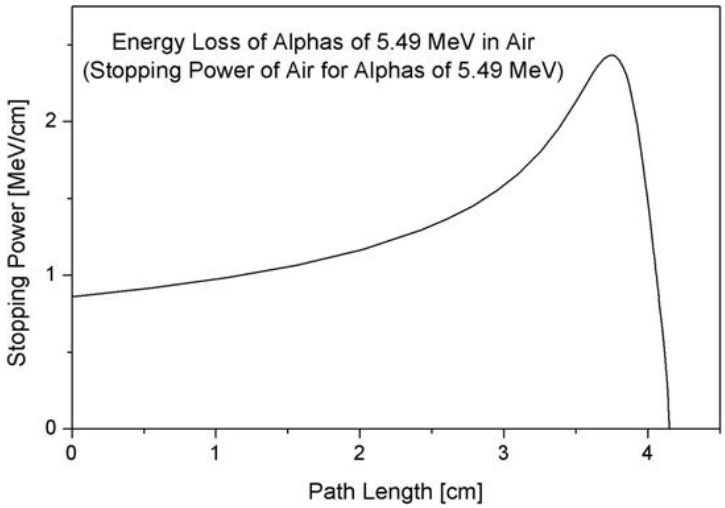

Figure 2.2: The energy loss of a 5.49 MeV alpha particle is given. The peak in energy deposition is the moment just before the alpha particle comes to rest, this is called the Bragg peak. Image retrieved from [14].

Due to the short range of alpha particles in tissue and high energy deposition the Linear Energy Transfer (LET) is typically high. The mean energy deposition of alpha particles are in the range of up to 100 KeV/μm. This means that much lower particle emissions are required in order to terminate cancer cells. The cytotoxicity, the degree to which a substance can cause damage to a (tumour) cell, of alpha particles is therefore much more effective than beta-emissions [18, 19].

2.2.1. Targeted Alpha Therapy

An interesting technique to deposit alpha particles directly on site at tumour cells is called Targeted Alpha Therapy (TAT). This technique uses tumour selective molecules (targetting vectors) which are coupled to an alpha-emitting radionuclide. The tumour selective molecules, such as antibodies or peptides, target the tumour cells as these cells are recognised through specific antigens that are present at the surface of tumour cells. The mechanism is similar to a key fitting into a lock, being a unique combination of donor and recipient [20]. The mechanism is imaged in figure 2.3. TAT is very effective in destroying metastases, which are challenging to treat by nowadays existing techniques [5].

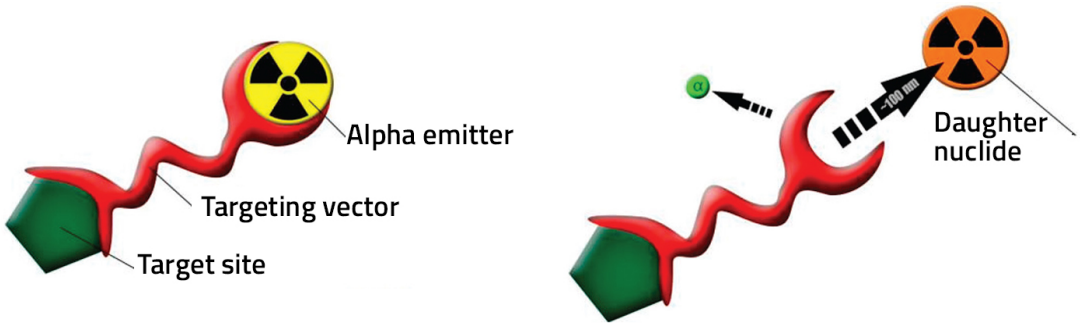

Figure 2.3: Schematic representation of the working mechanism of TAT. Upon disintegration the daughter nuclide traverses some distance due to recoil energy, this can be an issue when the daughter nuclide is not stable and disintegrates as the emitted ionizing radiation is now further away from target site. Image retrieved from [5].

2.2.2. Suitable Radionuclides for TAT and Recoil of Daughter Atoms

In the search for the perfect alpha-emitting radionuclide for TAT a lot of parameters need to be thought of: physical and nuclear properties of the radionuclide, the choice of tumour selective molecule that operates as a transport mechanism for radionuclides to tumour cells (in medicine this is called a targeting vector), and chelating (bonding) to bind the radionuclide to the targeting vectors [21]. There are a few hundreds of radionuclides which disintegrate via alpha-decay, but only few of them are useful for TAT. For example the half life of the alpha-emitter is only allowed in a certain interval, as a very short lifetime does not allow for production and delivery of the radionuclide to tumour site. On the contrary a half-life which is rather long is also not favourable as this allows for undesired dose to the patient. The following radionuclides are often used in TAT studies:

^{211}At, ($\tau_{0.5}$ = 7.2 hours).
Astatine-211 is one of the most studied radionuclides as it has a favourable half life and it decays solely via alpha decay and electron capture (2 routes possible) [22]. The main disadvantage of this radionuclide is that availability is limited, as production is only possible via cyclotron technology [23]. Moreover, radiolabeling of the isotope is challenging [24].

^{212}Bi, ($\tau_{0.5}$ = 60.7 minutes).
Bismuth-212 is a naturally occurring radionuclide and decays by 2 possible routes to an alpha, a β^- and a high energetic gamma of 2.6 MeV (only in decay of Thallium-208) [20].

^{213}Bi, ($\tau_{0.5}$ = 45.6 minutes).
Bismuth-213 decays via 1 alpha particle accompanied by a 440 KeV gamma. In spite of its short half life this radionuclide is the most used nuclide for TAT in clinical trials so far [25].

^{223}Ra, ($\tau_{0.5}$ = 11.4 days).
Radium-223 decays via a set of 4 alpha, 2 β^- particles and few gamma's ((energy range of 0.01 - 1.27 MeV). This radionuclide is not able to chelate with targeting vectors and therefore wide use is unlikely unless other methods for chelation are found [21]. However, some clinical applications are still possible as the inherent chemistry of the radionuclide is similar to calcium. Being an alkaline earth metal, both will have great tendency to accumulate in bone mineralization sites. Therefore ^{223}Ra is an interesting radionuclide in the clinical studies of bone metastases [4, 20].

^{225}Ac, ($\tau_{0.5}$ = 10 days).
Actinium-225 is characterized by a rapid decay cascade which is given in figure 2.4. The decay chain includes 4 alpha's, $2\beta^-$ and several gamma's (most occurring gamma's are 0.22 and 0.44 MeV [26]). Just as Radium-223 the half-life is relatively long, and in both decay chains 4 alpha's are emitted. This makes both radionuclides interesting for the use in TAT. However, unlike Radium-223, Actinium-225 does have favorable chelating properties making it a frequently used radionuclide in clinical studies [27]. The biggest challenge in the use of Actinium-225 for TAT is to retain the daughters of ^{225}Ac at the tumour site. Due to recoil effects the progeny of Actinium-225 can escape the targeting vector and migrate to other tissues in the body [5, 28].

The use of Actinium-225 in medical applications for TAT can be very interesting if all 4 alpha's in the decay chain of the parent nuclide will stay near the tumour site. However, upon disintegration the daughter atoms receive recoil (kinetic) energy. Excess energy, Q in equation 2.5, being released in the disintegration of the parent nucleus is transferred both to the alpha particle and to the daughter atom. For the disintegration of the following alpha decay we will calculate the recoil energy.

$$ {}^{A}_{Z}P \rightarrow {}^{A-4}_{Z-2}D + {}^{4}_{2}\alpha + Q \tag{2.5} $$

In equation 2.5 P is the parent radionuclide, D the daughter radionuclide, α being a Helium^{2+} atom and Q the excess energy. By conservation of momentum the relation for recoil energy of the daughter atom can be calculated and by rewriting the formulation for kinetic energy of the alpha particle we can obtain an expression for the kinetic energy of the daughter atom:

$$ m_\alpha \vec{v_\alpha} = -m_D \vec{v_D}, \quad v_D = \frac{m_\alpha}{m_D} v_\alpha \tag{2.6} $$

$$E_{k,\alpha} = \frac{1}{2} m_\alpha v_\alpha^2 = \frac{1}{2} m_D v_D^2 \frac{m_D}{m_\alpha} = E_{k,D} \frac{m_D}{m_\alpha} \rightarrow E_{k,D} = \frac{m_\alpha}{m_D} E_{k,\alpha} \tag{2.7}$$

In the decay of Actinium-225 the first daughter nuclide is Francium-221, the emitted alpha particle has kinetic energy of 5.8 MeV, atomic masses of alpha particle is 4 g/mol and atomic mass of francium is 221 g/mol. The calculation for the recoil energy of Francium-221 is given in equation 2.8.

$$E_{k,Fr-221} = \frac{4}{221} 5.8 MeV = 105 KeV \tag{2.8}$$

The recoil effect is often only a problem for alpha radiation. The recoil energy is energy and Z dependent, for beta radiation the mass of electron is much smaller than the mass of the daughter radionuclide so the recoil energy of the daughter radionuclide can often be neglected. However, if the atomic mass is relatively low and decay energy very high, then the recoil energy of a beta particle can be of significance.

In general for heavy radionuclides which disintegrate via alpha-decay the recoil energy is in order of 100 KeV. The binding energy of chemical compounds between radionuclide and targeting vector is in the order of eV's, thus the recoil energy that the daughter radionuclide obtains allows for bond-rupture and therefore the daughter radionuclide is released from the structure. Due to the recoil energy the daughter particle can on average cover 100 nm in tissue. When arrived in this phase the particle transport is affected by two other processes: diffusion and convection (blood flow). The diffusive regime plays a role if the radionuclide is at tissue or an organ, but often the convection regime plays a bigger role in the redistribution of the nuclide. The affinity for particular tissue of a radionuclide will decide where the radionuclide will end up [5].

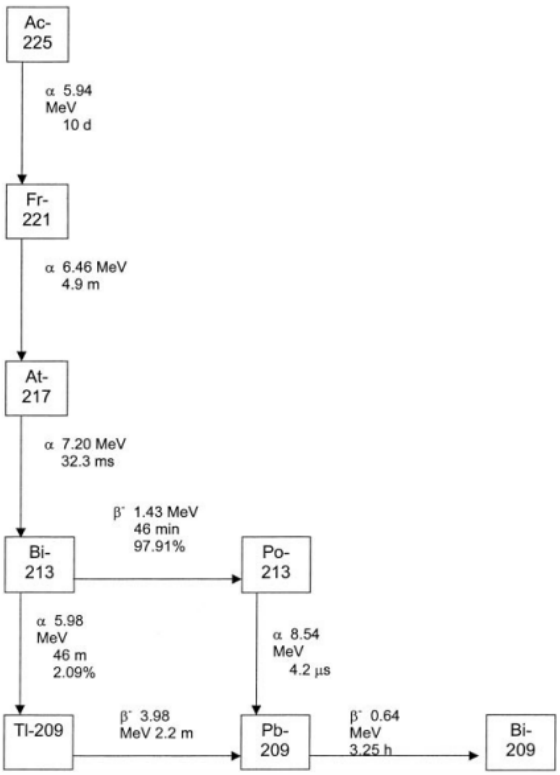

Figure 2.4: Decay chain of Actinium 225 which is characterised by 4 alpha particles and two beta particles. Bi-213 either decays to Ti-209 (alpha decay) or to Po-213 (beta decay). Both formed daughter radionuclides are unstable and decay to Pb-209. The emitted alpha particles are characterised by their decay energy. If one is able to measure the energy of such a particle, then information regarding the position of the parent radionuclide is gathered. With this information studies can be made regarding possible recoil effects of radionuclides in TAT.

2.3. Timepix Detector

The Timepix detector is a hybrid pixelated semiconducting detection technique where radiation is directly converted into charge carriers in the semiconducting layer, a pixel array beneath the semiconducting layer processes the charge carriers into an electric signal [8]. The technique is said to be hybrid as the semiconducting layer (the sensor) and electronic readout chip are produced separately. This means that both parts can be optimized individually from each other.

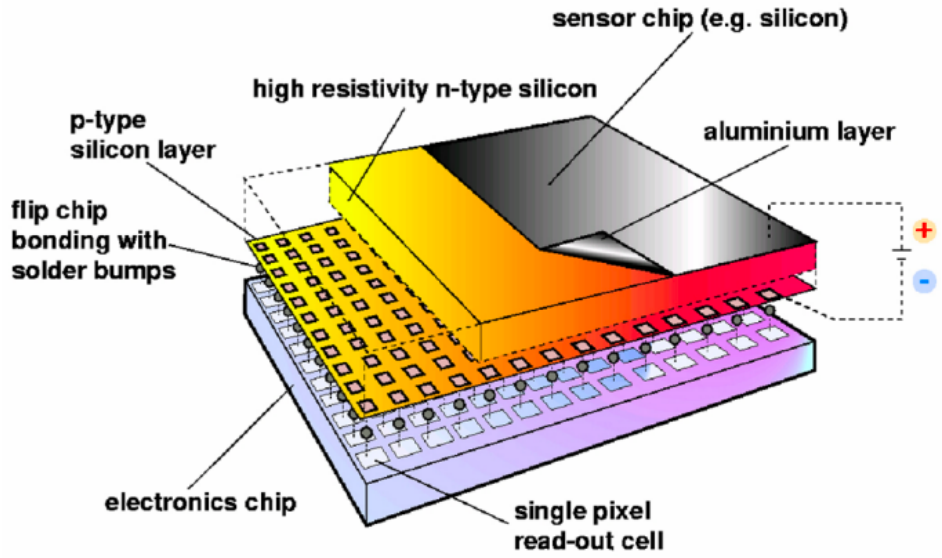

Figure 2.5: Schematic representation of Timepix technology. In the sensor material (often silicon) the radiation is directly converted into charge carriers. Due to an applied bias voltage the charge can be collected more efficient. Charge is collected at pixel sites, which are separated at a distance of 55 μm. Image retrieved from [29].

2.3.1. Origin of Timepix Family

The Timepix technology thanks its existence to the Large Hadron Collider (LHC) built at the European Organisation for Nuclear Research (CERN). The LHC is now in operations for over 13 years, but already back in the 80's physicist from CERN were developing pixel-sensors for the LHC which. These pixel-sensors, or microchips, could track the paths of electrically charged particles. When particles hit the sensor, it deposits a charge that is processed by electronics. These physicists questioned themselves what other applications these microchips could have. A prototype was born, the Medipix1. The device consisted of 64 x 64 pixels, with pixel size of 170 μm in both length and width. The device logic is very similar to that of an electronic camera. When the shutter is opened the device registers incoming hits on each pixel and in this way an image is formed. The technology has proven to do outstanding work in the field of single-photon counting [30]. In the design of the commercially available Medipix2 family some requirements had to be fulfilled, such as the spatial resolution which was limited by the 170 x 170 μm pixel size. In the new design the medipix2 family the pixel size was reduced to 55 x 55 μm while the total number of pixels on the device drastically increased, the new chip consisted of 256 x 256 pixels. Moreover, the readout was much faster and the pre-amplifier was now sensitive to both positive and negative charges [29].

The new Medipix2 family consisted of two devices, the first being the Medipix2 chip. As mentioned this chip operates as a normal electronic camera, during the time the shutter is opened incoming hits are counted. This technology works particularly well as a system to detect single-photons. The second device which originated from the Medipix2 family is the Timepix, this device is almost identical to the Medipix2 chip but a subtle change is the addition of several operating modes. These modes are discussed in paragraph 2.3.5, but by changing the counter function from particle counting to counting the arrival time it was possible to identify individual charged particles. Moreover, during the design phase the Time over Threshold (TOT) mode was incorporated such that it was possible to measure the energy of incoming radiation.

Nowadays the Timepix and Medipix2 detectors are already deprecated. At the time of writing the most recent chip in the Medipix and Timepix family is the Timepix3. The Timepix3 chip also consists of 256 x 256, each 55 xx μm, pixels but the readout architecture has better performance. The signal at pixel site is now continuously sent to processors such that the Timepix3 chip has no dead time. Moreover the time resolution has increased from 10 nanoseconds to 1.5 nanoseconds and noise has been minimised compared to the Timepix chip.

Timepix technology is used all over the world and has applications in multiple industries. The technology is most frequent used in medical imaging / dosimetry, but also has space applications [31] and the technology is used in material studies to determine the authenticity of art [32].

2.3.2. Architecture of Timepix

The Timepix detector consists of two main components: the silicon sensor material where radiation is converted into charge carriers, and the readout component which stores charge carriers to convert it into an observable signal. As can be seen in figure 2.6 on top of the sensor a backside metalization is placed. This has two main functions, first being to slow down the particle such that the kinetic energy is much lower. Especially in alpha-imaging applications the incidental kinetic energy of the particle causes a lot of interaction with sensor. The cluster size of the pixels that such an event has will be enormous, to minimize this cluster size an aluminum backside works very well. The second function of the backside metalization is that it functions as an electrode to apply a bias voltage over the sensor, the pixels then function as the grounded electrode. The bias voltage can be alternated such that the charges are more or less distributed over adjacent pixels (charge sharing effect), more information on this will follow later on in section 2.3.4. In our project the backside metalization is a 1 μm thick layer of aluminum mounted on top of the semiconducting sensor material. Different types of sensor material are available, but most frequently used material in Timepix studies is silicon. For better performance in the range of higher energy X-rays or gamma's (> 50 KeV) a sensor material with higher atomic mass can be used, such as GaAs or CdTe [33, 34].

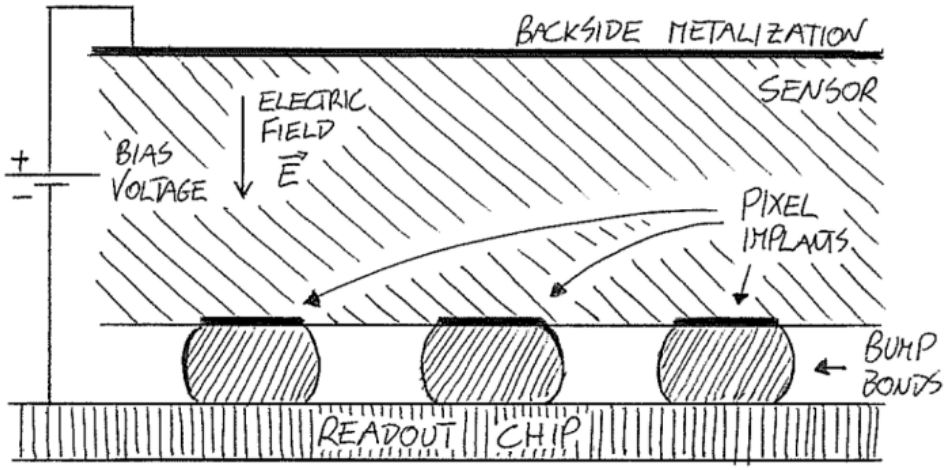

Figure 2.6: Schematic representation of Timepix technology. In the sensor material (often silicon) the radiation is directly converted into charge carriers. Due to an applied bias voltage the charge can be collected more efficient. Charge is collected at pixel sites, which are separated at a distance of 55 μm. Image retrieved from [35].

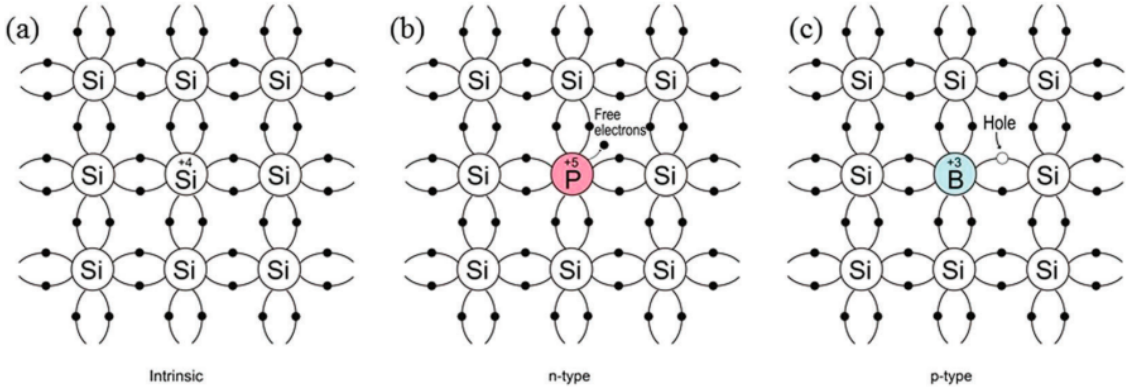

Figure 2.7: Representation of intrinsic silicon (a), n type (b) and p type (c) silicon. Donor and acceptor impurities are placed in a semiconductor to enhance conductivity and thus increasing performance of the system. Image retrieved from [36].

As can be seen from figure 2.5 the sensor material is n-type. For n type silicon an impurity element (dopant) with one more valence electron than silicon is added to the lattice structure. This electron can not form a pair bond as there are no adjacent valence electrons in the lattice. The extra electron causes the conductivity of the semiconductor to increase. The impurities in n type silicon are called donor states. Right above the single pixels the silicon has been made p type. For p type silicon the dopant has one less valence band electron, thus leaving open a vacancy (hole). An electron in an electron pair bond which is in the vicinity of the hole could absorb enough energy to break its bond and thus to fill the hole. So in the presence of holes, electrons are encouraged to flow and thus conductivity is increased [37]. The impurities in p type silicon are called acceptor atoms, as electrons are accepted at the site. A schematic representation of the excess electrons (n type) and vacancy / hole (p type) is represented in figure 2.7.

2.3.3. Radiation-Silicon Interactions

When ionizing radiation enters the silicon sensor of the Timepix it immediately starts to interact with the environment it moves through. Energy is released in the silicon sensor if the incoming radiation has sufficient energy to ionize silicon atoms. An electron in the valence band of silicon is transferred to the conduction band, leaving an empty vacancy (hole) behind. Although the band gap of silicon is 1.12 eV, the average ionization energy of silicon is 3.6 eV. This is due to the fact that 70 % of ionization energy is transformed in phonon excitation [38, 39]. If an alpha of 3.6 MeV is interacting with the silicon material you can expect that on average a million charge carriers are generated before the alpha has a net momentum of zero.

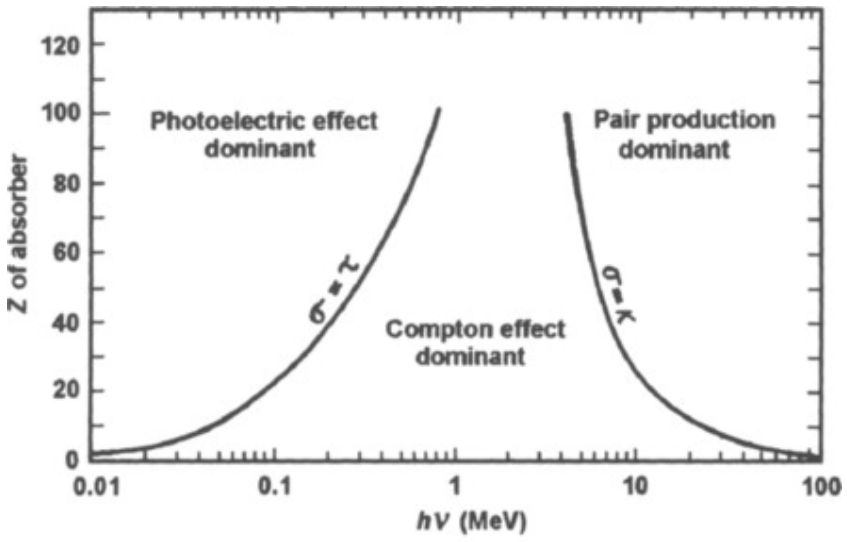

Figure 2.8: Interaction mechanisms of photons with matter depending on atomic number (Z) and energy of photon, expressed in MeV. Image retrieved from [40].

For the interactions of radiation with semiconducting material we can distinguish radiation into directly and indirectly ionizing radiation. Direct ionizing radiation is charged, such as heavy charged particles (alpha's) or kinetic electrons (beta's). Indirect ionizing radiation include x-ray, gamma's and neutrons.

Heavy charged particles:
Heavy charged particles mainly interact with silicon through inelastic collisions. These inelastic collisions are caused by coulomb forces between the positively charged particle and the (negatively charged) outer shell orbit electrons of silicon. An alpha particles ionizes the silicon by kicking an outer shell electron of silicon out of it's orbit. The energy that is transferred is the ionization energy (3.6 eV). As explained in the previous paragraph an alpha of several MeV's will cause millions of interactions while travelling through the silicon. The alpha track is unaltered by the interaction with an electron as the mass of alpha radiation is much higher than the mass of electrons, as we have seen in paragraph 2.1.3. The deposited energy of alpha radiation in matter can be represented by the Bragg curve, as seen in figure 2.2. More information about the tracks of alpha radiation in silicon will be explained in paragraph 2.3.4.

Beta interactions:
Beta- radiation, or fast (kinetic) electrons, strongly interact with orbital electrons. Because their mass (and charge) is equal to orbital electrons the beta radiation can be strongly deflected by coulomb interactions. Kinetic electrons can interact with silicon either via elastic collisions, or inelastic. Elastic collisions are not relevant in charge carrier transport as for elastic collisions there is no energy transfer, and thus no charge carriers are created. Therefore we will focus on the inelastic collisions. First interaction type is the interaction of fast electrons with the nucleus the nucleus, this type of interaction results in Bremsstrahlung [37, 41]. This type of interaction slows down and changes the direction of the fast electron. The energy lost by the fast electron is being released as a photon. The second interaction type is the interaction of fast electrons with orbital electrons of silicon. These interactions results in energy transfer from fast electron to orbital electron. Charge carriers are created if the fast electron ionizes the silicon.

Gamma and x-ray interaction:
Gamma and x-ray radiation are uncharged radiation and therefore do not interact via coulomb forces. Gamma (photons from nucleus interactions) and x-ray (photons from orbital electron interactions) both interact mainly via the photoelectric effect, Compton scattering and pair production. Depending on the Z-value (atomic number / proton number) of absorber and photon energy. As can be seen from figure 2.8 the dominant regimes for photon interaction with silicon (Z = 14) with photon energies of several KeV to some MeV are the photoelectric effect and Compton effect. In the photoelectric effect the incident photon interacts with the silicon orbital electron. The incident photon is completely absorbed the orbital electron, giving it enough energy to be ejected from the orbit and thus now is a free electron. For the Compton effect the incident photon transfers some of its energy to the orbit electron, the photon is deflected over some angle θ. The deflected photon has transferred some of its energy to the orbital electron, which now has enough energy to escape the orbit of silicon and can be considered as a free electron.

2.3.4. Charge Collection in Timepix

Once the direct and indirect ionizing radiation has caused the formation of electron-hole pairs in the silicon the charges must be separated. If nothing would be done to the system the charges would recombine which means a loss of signal. Recombination of the charges is prevented by applying an electric field over the system. This electric field separates the charges as the charges drift in opposite directions. The charge carrier transport is thus influenced by the drift of holes and electrons induced by the externally applied electric field. Besides drift, charge carrier transport is also influenced by diffusion in the sensor material. Moreover, coulomb interactions strongly influence the carrier transport. The charge carriers interact among each other due to electrostatic forces, the cloud of the charge carriers is drifting towards the collection electrodes. The cloud is thus expanding not only by diffusion, but also by coulomb forces [35].

Depending on the type of radiation different charge sharing effects can be expected. As mentioned before, alpha particles will cause millions of ionizations. The charge cloud that such a particle will induce will experience great coulomb forces. Moreover, the range of alpha particles in silicon are short ranged and can be calculated as described by J.W. Poston [42]:

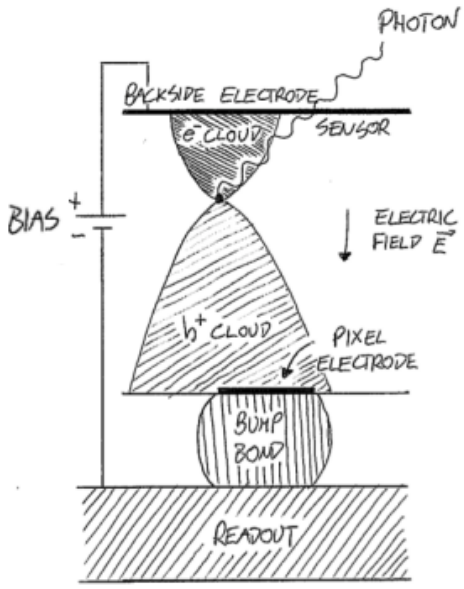

Figure 2.9: Charge carrier creation by incident photon in silicon absorber. Holes and electrons are separated by an externally applied electric field. Once created, the charge carrier cloud starts to expand due to diffusion and coulomb forces. For photons that are absorbed deep in the silicon or near the pixel electrode, the charge cloud hardly plays an effect in charge sharing. For photons absorbed far away from the pixel electrode charge sharing among several pixel electrodes play a bigger role. Figure retrieved from [35].

For an alpha particle of 4-8 MeV:

$$R_{cm} = 1.24E_{MeV} - 2.62 \tag{2.9}$$

Considering an alpha particle of 5.5 MeV, its range in air is 4.2 cm. Now the range of a 5.5 MeV alpha particle in silicon can be calculated by the relation:

$$R_{air} \times \rho_{air} = R_{Si} \times \rho_{Si} \tag{2.10}$$

Now, $\rho_{air} = 1.225\times 10^{-3} g/cm^3$ and $\rho_{Si} = 2.33 g/cm^3$. Thus by equation 2.9 and 2.10 the range of a 5.5 MeV in silicon is 22 μm. The silicon sensor is 300 μm thick, thus an alpha particle will deposit all its energy at the beginning of the sensor material. The charge cloud induced by an alpha particle therefore will expand rather much compared to photons, and the charge cloud will be distributed among several pixel electrodes. This effect is known as charge sharing effect and can also be seen for photons, as is depicted in figure 2.9. The output for alpha, beta and photons are depicted in figure 2.10. The charge sharing effect can clearly be seen for alpha and beta radiation.

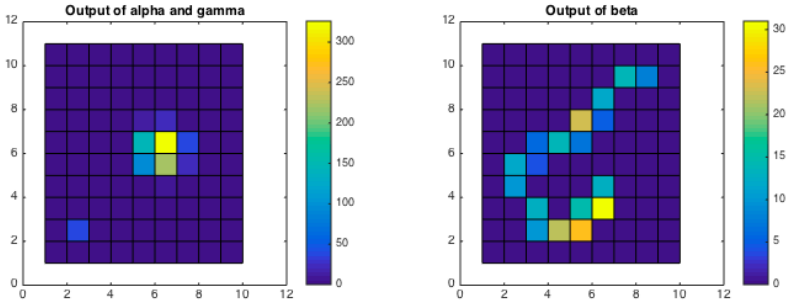

Figure 2.10: Output of pixels for alpha, beta and gamma radiation analysed in Matlab [43]. In the left figure both the output of a gamma and an alpha are seen. Output of both alpha and beta particles clearly show the influence of the charge sharing effect. For alpha particles this is particularly due to the expanding charge carrier cloud, while for a beta particle this is due to the 'random walk' caused by electrostatic forces of the incident fast electron with orbital electrons.

2.3.5. Operating Modes of Timepix

Unlike the Medipix family, Timepix can operate in three modes: counting mode, time of arrival (TOA), and time over threshold (TOT). The counting mode is the mode the system behaves identical to the Medipix 2 system. The pixels register incoming particles each time the signal surpasses the threshold, each of such an event is registered and thus the particles can be counted. In the TOA mode the pixels registers the time when the charge carrier signal exceeds the threshold. Output of this system is continuous after the pulse has been registered, and is only shut of once the shutter has closed. The TOA mode can thus be used to measure the moment off incidence of a charged particle that displays a difficult to read image as data. In TOT mode the pixels register the duration a pulse is above the threshold. The total number of counts of timestamps is then a measure for the incoming particle energy. The TOT mode can thus be used to measure deposited energy of radiation.

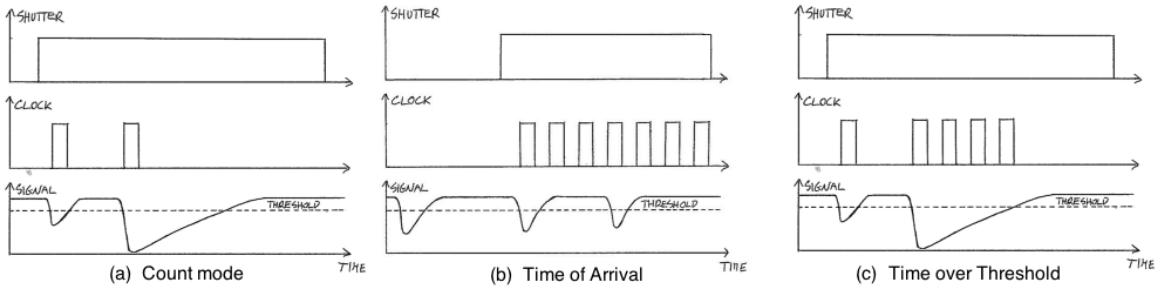

Figure 2.11: Operating modes of Timepix. The count mode does only count the number of times a signal is above threshold, while TOA and TOT give more information regarding energy and timestamps of the signal. Image retrieved from [35].

The new Timepix system, the Timepix 3, can both measure in TOT and TOA mode simultaneously. Thus measuring its energy and moment of incidence of incoming (charged) particle.

3

Methods

In order to propose a method to find answers to the proposed questions in the goal of the research certain skills needed to be learned. Skills such as the relevant know-how of the Timepix system, its variables, its operating modes and the response of the system and also the ability to compute the output files. These skills were acquired by performing several measurements, such as the calibration of an alpha source of Erasmus MC. These experiments will elaborated further on in section 3.1, and in chapter 4. Data analysis was performed in Matlab [43], the proposed mechanisms of this analysis is described in section 3.2.

3.1. Experimental Method

All experiments were performed at the Reactor Institute Delft (RID) with a Timepix quad chip detector (4 chips of 256×256 pixels each). The RID is in possession of a 409 KBq Am-241 source, which is a 5.5 MeV alpha emitter. This source has been used in most experiments. A basic experimental set-up is given in figure 3.1. In this work, 4 major measurements have been performed. The first two being the introduction projects: the calibration of an alpha emitting source from Erasmus MC, and the imaging of alpha particles in spheroids emitted from the decay chain of Ac-225. Knowledge and skills that were gathered from these projects were used in the two big projects of this thesis: The spatial resolution measurements of the Timepix chip, and the Energy resolution measurements of the chip. All experiments will be briefly discussed in this chapter, further motivation is discussed in chapter 4.

Calibration of Erasmus MC source:
Erasmus MC is in possession of a 3.7 MBq Am-241 source which was used for dosimetry purposes. The source was placed in a collimator (see figure 3.2 A). The proposed question from Erasmus MC was how many particles were counted at a distance of 2.5 millimeter from the collimator. The experimental set-up for these experiments is given in figure 3.1. In these experiments the Timepix chip was mounted to a frame while the

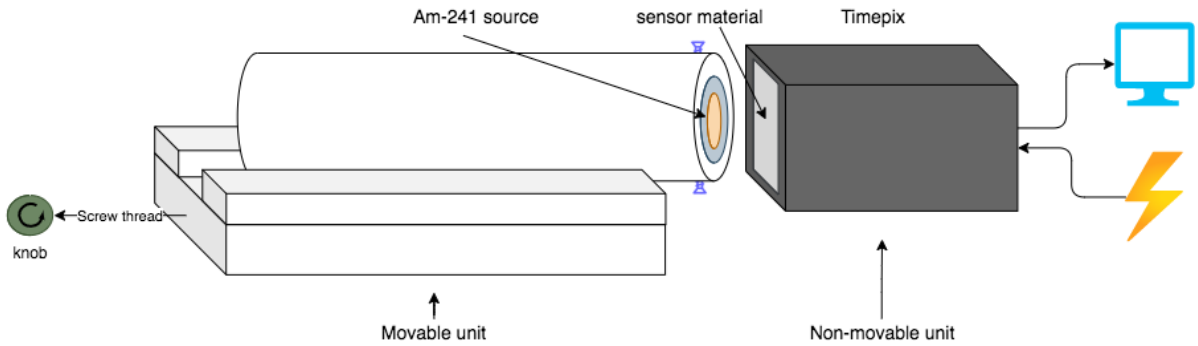

Figure 3.1: Schematic representation of the introduction project: calibration of a 3.70 MBq source. The source was placed inside a hollow cylinder. In this set-up the Timepix chip was placed at a fixed location, while the cylinder + source could be moved perpendicularly w.r.t. the Timepix chip. By turning the knob a full rotation the source was displaced 1 millimeter.

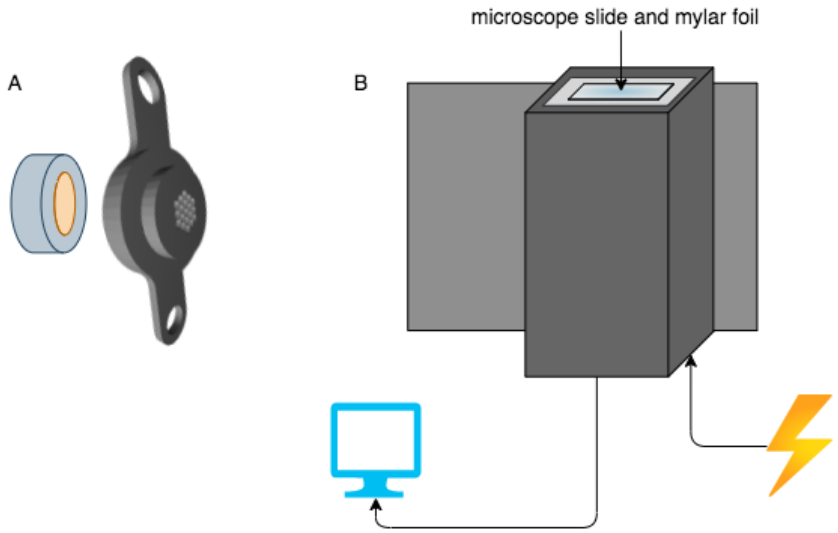

Figure 3.2: Schematic representation of the used source and collimator in the calibration measurements (A), and used set-up in measurements of imaging alpha particles in spheroids (B). The overall diameter of the source in figure A is 12.7 mm, which gives a sense of length of scale the collimator. The samples in figure B are directly put on the sensor material, only divided by two layers of Mylar foil.

Americium-241 source of either Erasmus MC or RID was placed and mounted in a cylinder, which was able to move perpendicularly w.r.t. the sensor material. Multiple measurements with both Erasmus MC source and RID source were performed in counting mode.

Imaging alpha particles in spheroids
Spheroids implemented with Ac-225 were acquired and were sliced in layers of 20 μm thick. The slices were put on a microscope slide, and covered with 1.8 μm Mylar foil. Each slide contained only several Bq of activity. The samples were put on an extra layer of Mylar foil, before being put on top of the Timepix on the sensor material. The experimental set-up is given in figure 3.2. Several measurements were performed with the acquired slices in counting mode.

Spatial resolution measurements
The spatial resolution measurements were performed with a collimator. Holes of the collimator are 25 μm, and the pitch is 32 μm (distance from center of hole to neighboring center of hole). The experimental set-up is much alike the set-up of experiments of imaging alpha particles in spheroids. Instead of a microscope slide, the collimator was placed on the chip. On top of the collimator an object (microscope glass and copper) with a fine edge was placed, see figure 3.3 A & B. The Am-241 source was held just above the chip.

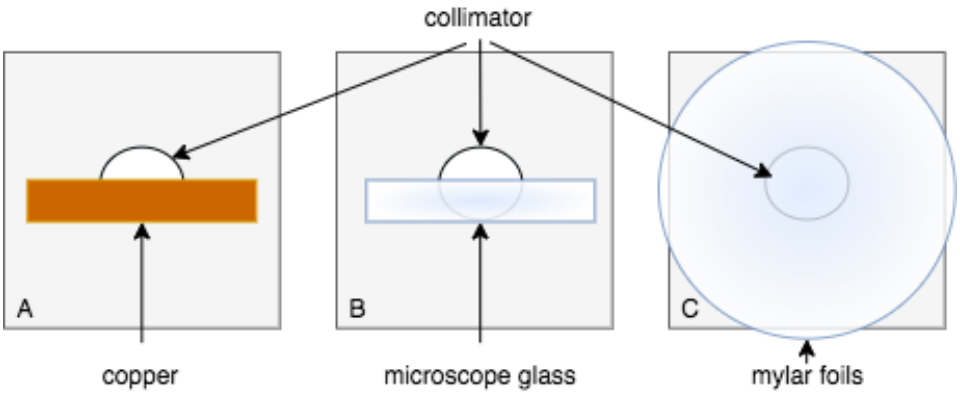

Figure 3.3: Top view of the sensor material of the Timepix chip for the place resolution measurements (figures A and B) and the energy resolution measurements (figure C). All measurements were performed with a collimator such that the particle 'beam' emitted from the source would be approximately monochromatic.

Energy resolution measurements

The experiments of energy resolution were performed in the set-up described in figure 3.3 C. The collimator with pitch of 32 μm was used. Several disks covered with layers of 0 to 7 Mylar foils were prepared. The disks were put on top of the edges of the chip. The alpha source used in this experiment was not the same used in previous experiment. For this experiment an old fire smoke detector was used, which incorporated a 33 KBq Am-241 source. The source was held by a clamp and was positioned right above the disk with Mylar foils. Images of this set-up are given in figure 3.4.

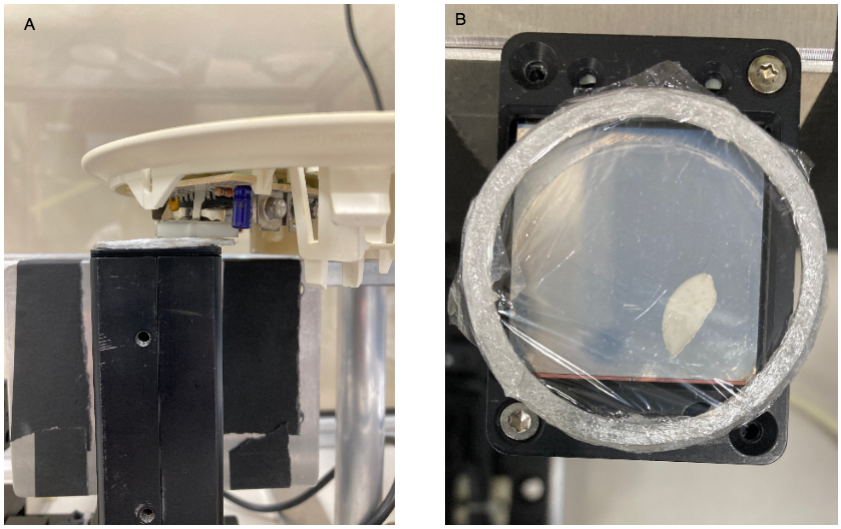

Figure 3.4: Set-up for energy resolution experiments from side (figure A) and top view (figure B). 8 rings covered with 0 to 7 Mylar foils were prepared for the experiments. The collimator with pitch of 32 μm and L/D of 20 was used.

3.2. Computational Method

All data analysis was performed in Matlab. To be able to understand the data a lot of time has been spend in developing scripts. This report will not put its focus too deep into these scripts, but the development of these scripts will be highlighted:

Counting mode

The first set of experiments were performed in the counting mode. As explained in section 2.3.5, in this mode the number of particles were counted and each pixel indicated the number of times the signal exceeded the threshold within the shutter time. As can be seen from figure 3.5, the script analysed the output of each pixel separately in a chronological order. If the output of the cell, and three of its neighbors, were nonzero then the data was registered as an alpha particle. The coordinates of the cells were registered and the position of the alpha particle was calculated by:

$$X_\alpha = \frac{\sum_i P(i)(x_{pixel}(i) + y_{pixel}(i))}{\sum_i P(i)} \tag{3.1}$$

In which P(i) was the value of the pixel cell (to account for multiple hits within the shutter time), x_{pixel} and y_{pixel} were the pixel indices, and i was the number of cells involved.

Time over threshold mode

The position and energy resolution measurements were performed in TOT mode. In this mode the output of the system indicated the period of time the signal exceeded the threshold within the shutter time. Instead of analysing every single pixel cell, this script worked in the following manner: The maximum value of the 512×512 matrix was found, its nonzero neighboring pixel cells were found, coordinates and values of the pixel cells were saved after which all nonzero pixel cells that formed the alpha particle were put to zero. This loop was performed as many times as the threshold in the script obliged. A basic representation of the working of this script is represented in figure 3.5. Calculation of the positioning of the alpha particle was the same as in counting mode represented in equation 3.1.

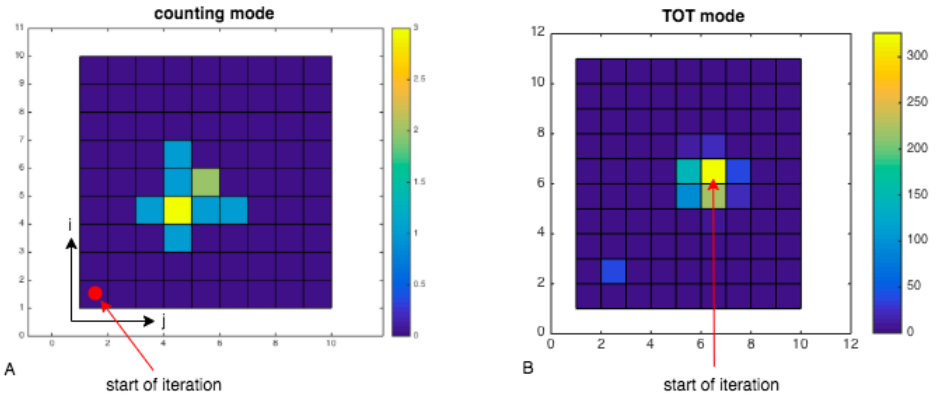

Figure 3.5: Approach of scripts for counting (fig. A) and TOT (fig. B) mode. The counting mode script analyses each single pixel, starting at (i,j) = (1,1) at which the script analyses if the value of the pixel fulfills the pre-set threshold. This is a time consuming process in analysis of data, the proposed script which was used in TOT mode fixed these problems.

Spatial resolution computations

In the experiments for the spatial resolutions the resolutions can be derived from the formed images from the experiments given in figures 3.3 A&B. When the alpha particles are counted and binned, it will be shaped as a step function as the intensity of the bin count gradually increases. From this data a Gaussian function is plotted, which is given by:

$$Ae^{-\frac{(x-B)^2}{(2C^2)}} \tag{3.2}$$

In which A and B are some constants and C is proportional to the full width halve maximum (FWHM), or the image resolution:

$$\text{Resolution} = \text{FWHM} = 2\sqrt{2ln(2)} \times C \tag{3.3}$$

At the start of the iterations at first some random numbers for A, B & C are implemented. The Gaussian function is fitted with these parameters. When integrated, the Gaussian function forms a step function. Now, the integrated Gaussian function can be compared to the binned data:

$$\text{Err(i)} = \frac{\text{bin(i)} - \text{Integrated Gauss(i)}}{\sqrt{bin(i)}} \tag{3.4}$$

For which bin(i) is the number of alpha particles in bin i. By varying the parameters A, B & C the summed error of the fit compared to the binned data can be minimised. In this way the optimum values of A, B & C are found. Working of the above mentioned method is represented in figure 3.6.

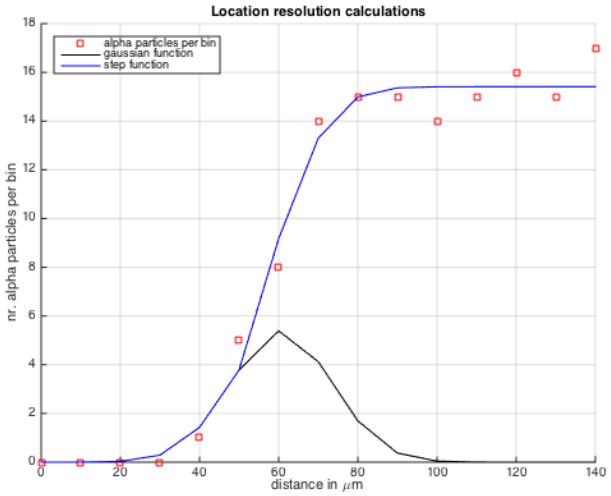

Figure 3.6: Spatial resolution of a Timepix chip can be calculated by finding the FWHM. In this figure some experimental data is given for clarity's sake. For this data the FWHM, or the location resolution of this image, is about 30 μm.

Energy resolution computations

In the energy resolution measurements the TOT value of a single alpha particle is registered. The measurement will run for a finite time such that few thousands of alpha particles are counted. It is expected that the distribution of the TOT value of all these counted alpha particles is Gaussian shaped. Just as for the spatial resolution measurements the resolution of such a Gaussian function can be determined by calculating the Full Width at Halve Maximum (FWHM). The energy resolution is then calculated by equation 3.3, only now the unit of the resolution is in MeV.

4

Results and Discussion

In this chapter the results of both introduction projects and resolution projects are given and discussed. The introduction projects, given in paragraph 4.1 and 4.2 helped in gaining useful knowledge and experience of Timepix operation.

4.1. Am-241 Source Calibration

For clarity's sake the configuration that was used in the experiments of the Americium-241 calibration is given in figure 4.2.B. The goal of these experiments was to determine the number of particles at 2.5 millimeter distance from a 3.7 MBq Am-241 source. The source was mounted in a collimator as a result of which a lot of alpha particles are absorbed by the collimator material.

The first set of experiments performed in the calibration project were performed with the Erasmus MC source and results are given in figure 4.1. Results were obtained for both with and without collimator by measuring the total number of particles that interacted with the Timepix chip. Measurements were performed over several distances in order to study the intensity decay.

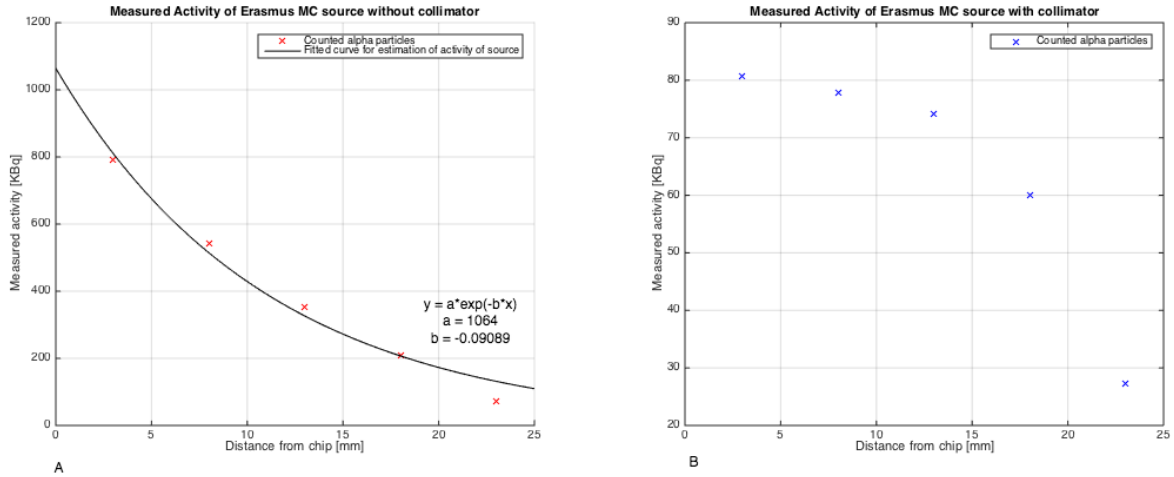

Figure 4.1: Results for Erasmus MC Am-241 source with (fig B) and without (fig A) collimator. Results for source + collimator show that activity slowly drops at first few millimeters. The fitted activity at the surface of the source does not match the known activity and thus this must be accounted for. All measurements are performed in counting mode.

The results for the source without collimator show a clear exponential decay. In figure 4.1.A. a curve has been fitted to calculate the activity at the absolute surface of the source. By comparing the true activity with the measured activity we can determine the detection efficiency of the system. Throughout the project of the source calibration we have worked with the following assumption: we treat the Americium-241 source of

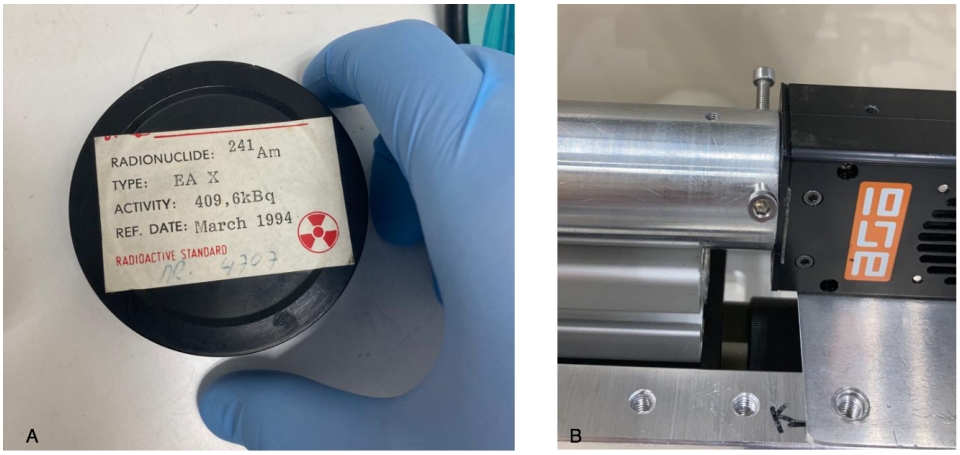

Figure 4.2: Image of the case of the Americium-241 source owned by the RID (figure A) and image of experimental set-up used in the experiments of calibration of the Americium-241 source of Erasmus MC (figure B).

both Erasmus MC and RID as perfect halve-sphere emitters. In this way, only 50% of all emitted alpha particles will arrive at the chip if the sources are placed right in front of the detector. In the decay of Am-241 only a very small fraction does not disintegrate via alpha decay (3.6×10^{-10} via spontaneous fission [44]), thus a supplemental fraction other decay types do not need to be included. The total correction factor for calculation the true activity at surface level is thus 2.

The activity of the source can be determined by correcting the fitted activity of the source at surface level by the correction factor. The activity at surface level is given in figure 4.1A. The true activity measured by the Timepix chip at the surface level is therefore 2.1 MBq. This is only 57% of the known activity of the Erasmus MC source (3.7 MBq) and thus the detection efficiency of the set-up used in this experiment is 57%. Results of this experiment showed that not all emitted particles are measured, so this arises an important question: is the efficiency of the Timepix chip only 57%? Or is this loss of particles implied by the measuring method? If this efficiency is known, only then an answer to the goal of this experiment can be formulated.

In order to study the efficiency of the used set-up two experiments have been performed. For the two available Am-241 sources the measured activity at the surface of the source had been fitted, results are given in figure 4.3. By equation 4.1 an estimation of the source's activity can be made.

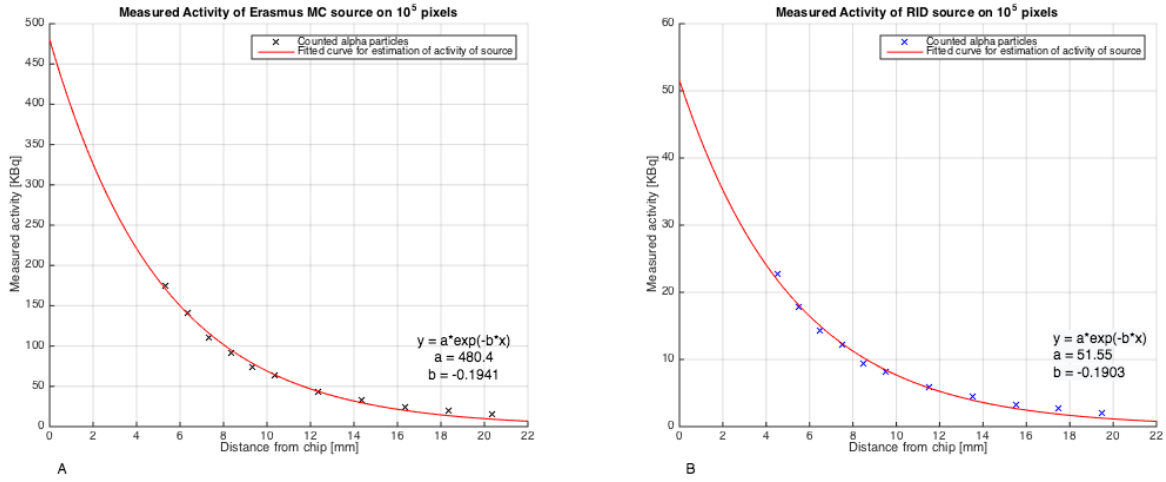

Figure 4.3: Results for Erasmus MC source (fig. A) on 100 × 100 pixels, and results for RID source (fig. B) on 100 × 100 pixels. For both experiments a curve has been fitted to calculate the activity on the surface of the sources.

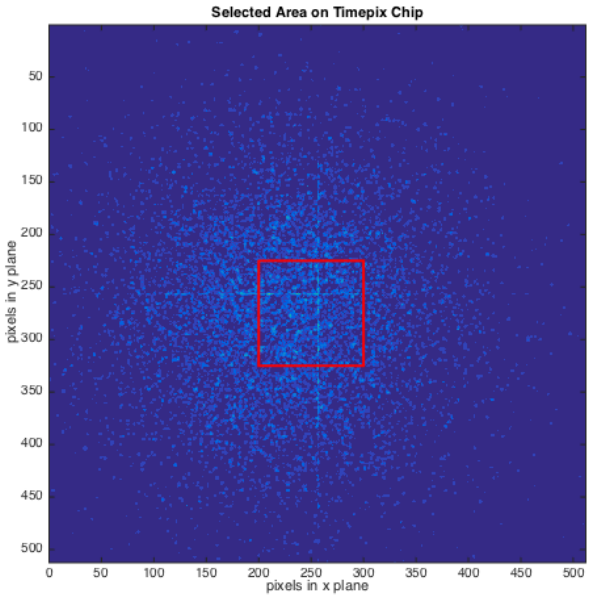

Figure 4.4: Data on Timepix chip after measurements with RID Am-241 source on 3 millimeter from chip. The selected pixel surface for calculations of activity is depicted with the red lines. The selected surface is 100 × 100 pixel, each of size 55 by 55 μm. Expansion of the particle cloud is visible already at 3 millimeters from the chip, as some particles are detected at the vicinity of the edges of the chip. For increasing distances the likelihood that particles are emitted along sides of the chip increases, thus limiting the signal.

Contrary to the experiments depicted in figure 4.1 we calculated the activity on the surface of the sources via another method. In the earlier measurements the geometrical expansion of alpha particles had not been accounted for. In other words: if the source is placed further away from the chip, then some alpha particles will miss the surface of the chip as the cloud is expanding. In order to tackle this problem another analytical method had been proposed: On the Timepix chip a certain area had been selected, in this area the intensity had been shown to be uniform and maximum. This is depicted in figure 4.4. Now, by comparing the surface of this selected pixel area with the surface of the source the activity could be estimated. The following relation was used in this approximation:

$$\text{Estimated Activity of source} = \text{Measured Activity} \times \frac{Area_{source}}{Area_{selected pixels}} \times \text{Correction Factor} \tag{4.1}$$

The selected area for these experiments is 100 × 100 pixels. The diameter of the sources are known and thus the estimated activity of the sources were calculated. For the RID source the activity was estimated at 3.2×10^2 KBq. This leads to a detecting efficiency of 79.0 %. For the Erasmus MC source the activity was estimated at 2.3×10^3 KBq, meaning a detecting efficiency of 60.9 %. These results show that the detecting efficiency of the set-up is different for both sources. A possible explanation is the influence of the detection

Measuring time (ms)	Activity [KBq]
0.05	20.47
0.10	20.30
0.20	19.60
0.50	19.34
1.00	19.10
2.00	18.78

Table 4.1: Results for different iteration intervals. All measurements were performed at 4.5 millimeters from the detector surface. The influence of the measurement time on the computed activity was questioned. However, results show that the size of interval in which is measured hardly plays a role. Only if the measurement time is increases significantly such that alpha particles overlap, then the measured activity will be significantly lower than the true activity.

time interval. In order to compute each particle as a singular particle, the time that is measured must be of such short interval that particles do not overlap. Therefore, for a higher activity of the source a shorter measurement time is needed.

In order to study the influence of the measurement time on the estimated activity on the surface of the sources a simple experiment has been performed. Results are given in table 4.1. In this experiment the RID source was placed in front of the Timepix chip, at a distance of 4.5 millimeters. For several measurement times the activity has been computed. The results show no influence of the measurement time on the counted activity. In hindsight this is an obvious observation, but for the sake of the experiment these tests had to be performed in order to check if the Timepix system counting efficiency would be affected by the measurement time.

As the measurement time does hardly influence the detection / counting efficiency of the system some other parameter must influence this. A possible explanation is the choice of selected area on the Timepix chip. This does seem to influence the results as the efficiency of experiments given in figure 4.3 are not alike. In proposing an answer to the goal of this sub-project we decided not to look at a certain area on the chip, but rather focus on the Erasmus MC source + the collimator. The particle beam that is emitted through the collimator is by approximation a monochromatic beam, thus the approximation for the geometrical expansion of the emitting sphere does not account for in this case as all particles traverse in a straight line to the Timepix chip interface.

Results given in figure 4.5 show the experiment where the source of Erasmus MC was placed in its collimator, while increasing the distance at which the source was placed. For the complete surface of the Timepix, given in figure 4.5A, there is hardly any loss of alpha particles up to a distance of 8 millimeters. Results of figure 4.5B shows the same experiment, but then a small pixel area has been selected to show the influence of this selection. Here the geometrical expansion still does play a role, but the choice for complete area of Timepix chip seems to have hardly any effect on counting output. The results show that at 2.5 millimeters from the Erasmus source + collimator around 82 KBq of activity of alpha particles are received.

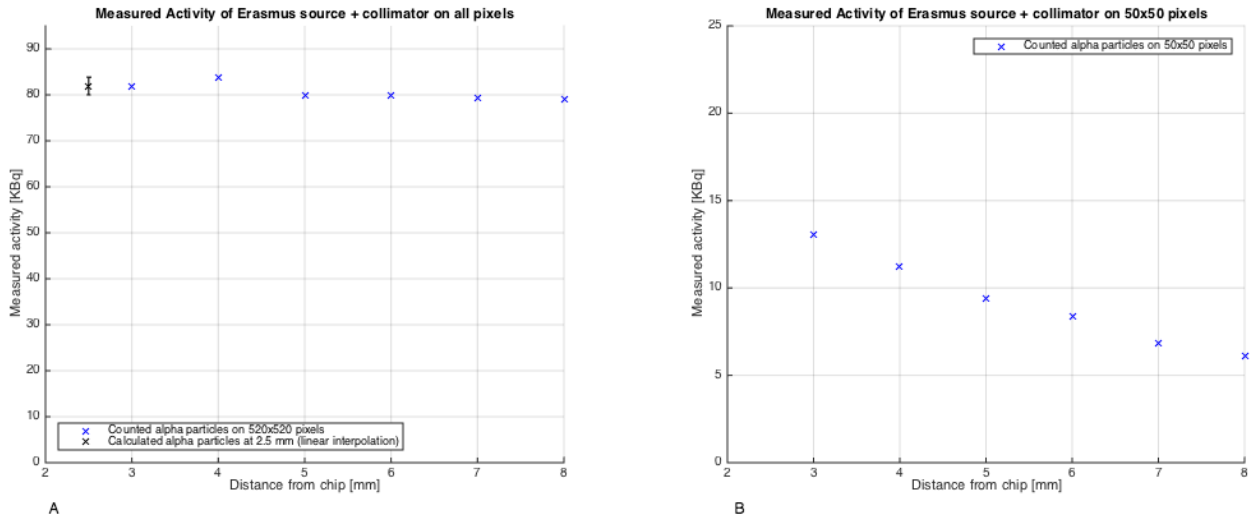

Figure 4.5: Results of Erasmus MC source + collimator, counted over complete Timepix surface (figure A) and selected pixels (figure B).

This project was very useful for further work performed in the thesis as a lot of experience with the Timepix chip and data processing was done.

4.2. Alpha Imaging in Spheroids

As discusses in paragraph 2.2.2 Actinium-225 is a very promising radionuclide in TAT studies as it decays via 4 alpha particles with all very suitable half lives. At the RID studies to the use of Ac-225 applied to tumour cells have been performed. A spheroid is a grown cluster of cancer (tumour) cells and is typically no larger than 600-700μm of size. In these experiments the chelating molecule DOTA was radiolabeled with Ac-225 and linked to iron nano-particles. It was expected that the solvent would accumulate at the edges of the spheroids. About 1% of the initial activity of the Ac-225 solvent, which is 10 KBq, is expected to accumulate in the cells. Slices of the spheroids (each 20 μm thick) were obtained and for each slice only a few Bq was expected.

The proposed question for this project is if we can image alpha particles in these slices. Moreover, can we tell where the alpha particles accumulate in the spheroid? The experimental set-up has been given in chapter 3. The slices are put on a microscope glass and are covered with a Mylar foil, the Mylar foil is then placed on top of the Timepix chip. Results for some samples are given in figure 4.6.

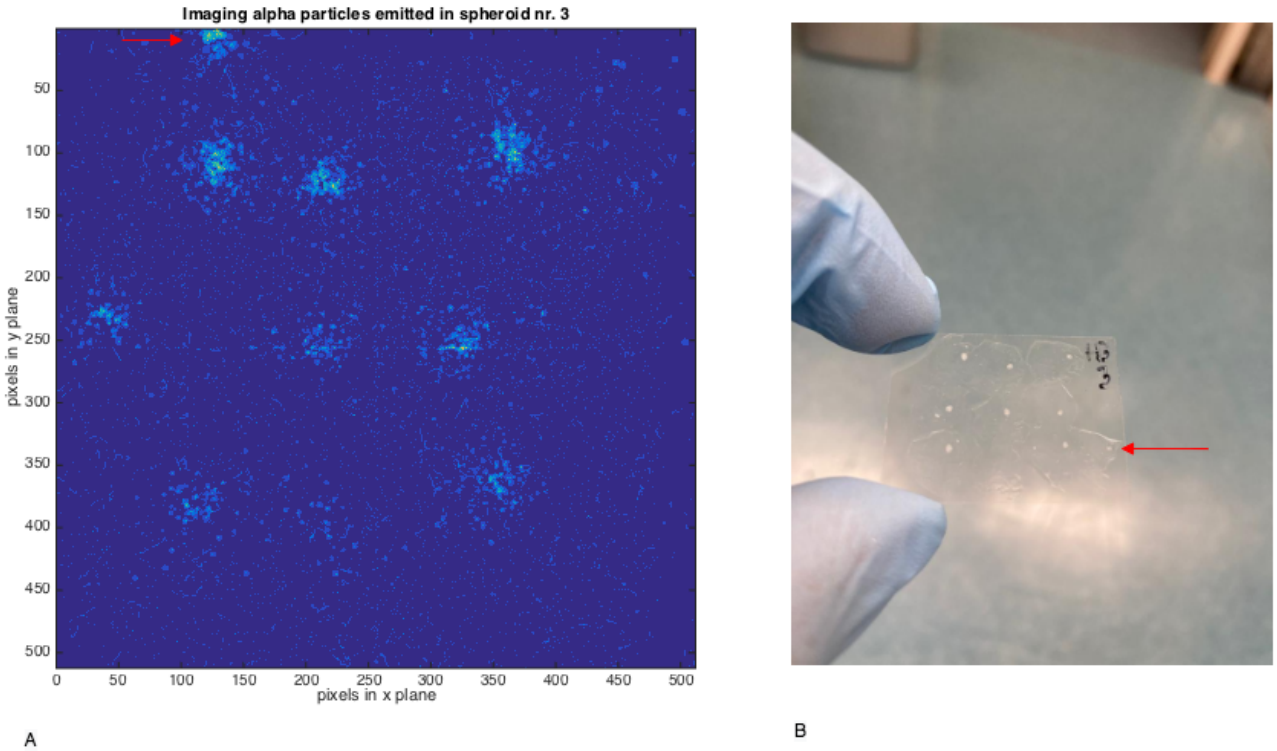

Figure 4.6: Output of Timepix from experiment with Ac-225 treated spheroids (figure A) and image of the used microscope slide and slices used for the experiment (figure B). In figure B the slices are seen as small white dots. In total 10 slices were placed at the microscope slide. Radiation emitted from the decay chain of Ac-225 is seen in figure A. All 10 slices clearly contain Ac-225 as in figure A we can see 10 radiation patterns in figure A. A red arrow is given in both figures as a frame of reference, so the slice at most southeast of figure B (see red arrow) is represented by the radiation emitted at most northwest in figure A (see red arrow). The measurement time was set to 60s per frame as the activity in the slices was only of order of few Bq. A longer measurement time on the Timepix chip causes more noise to the chip.

The results of this sample shows that each slice contains some alpha-emitting particles. There is some difference in intensity of activity and thus uptake of the Actinium-225 was not uniform. Results of another spheroid are given in figure 4.7. This figure also clearly shows that alpha particles can be imaged in biological samples. In the decay of Ac-225 4 alpha particles are emitted, and 2 beta particles. The beta particles are also imaged in both samples, and are given in figure 4.7 by the red arrows.

Imaging the alpha particles have proven to be possible. It is only rather hard to tell anything about the resolution of the system. The results show 'blobs' of alpha radiation over 50 pixels in width, which is about 2.5 millimeters. This is clearly larger than the size of spheroids so there is not a way to tell if the alpha particles

did in fact accumulate at the edges of the spheroid. It is plausible that the activity had been smeared out by cutting of the spheroids. Another influence in the big size of the intensity pattern is the fact that the alpha particles can traverse in 3D direction. We realized that in order to study the resolution of alpha particles on a Timepix system that we needed a collimator in order to ensure a monochromatic trajectory of the alpha particle. For these experiments it was however, not possible to perform measurements with the collimator as the intensity of the samples was too low.

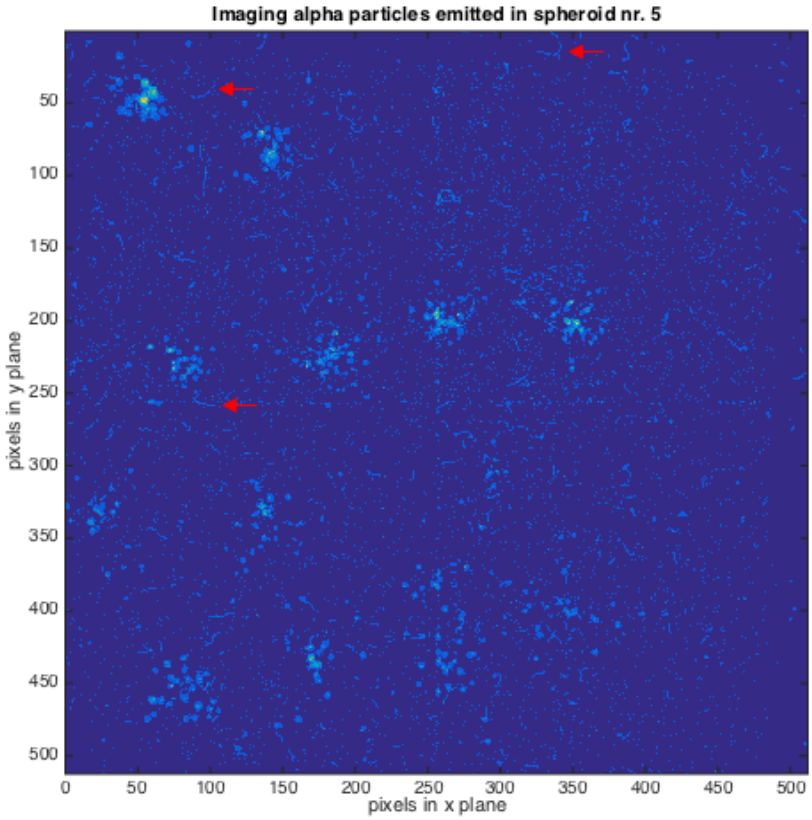

Figure 4.7: Image of obtained slices from spheroid nr. 5. The results show little less intensity than results showed in figure 4.6. In the figure beta particles are visible and are indicated by the red arrows.

During one of the experiments mentioned in this section the Timepix chip unfortunately broke. At the edges of the Timepix several wire bonds were damaged during the experiments. Most probably this happened during the placing of the sample on the detector. In hindsight our method was too rough and should have been more careful with the chip. The device was repaired by Amsterdam Scientific Instruments (ASI), which is an organisation which among other equipment sells Timepix technology. Beside the repair ASI showed us the abilities of the Timepix chip. In the experiments discussed so far we only used the counting mode. ASI suggested to mainly use the TOT mode as this mode gains extra useful data in experiments. As discussed in section 2.3.5 the TOT mode offers information on the extend of time a signal is above threshold. This information is especially useful in reconstructing the energy of the incoming particle that interacted with the chip. Moreover the TOT mode allows for better determination of positions of alpha particles as there is simply much more data per pixel such that the relative error is much smaller.

4.3. Spatial Resolution of Timepix in Alpha Imaging

In order to study the spatial resolution of the Timepix chip as a response to alpha radiation several experiments were performed. The experimental set-up of the location resolution measurements has been given in figures 3.3 A&B. The method to calculate the spatial resolution of the Timepix system is described in section 3.2. The first set of experiments for this subject have been performed with a collimator which had holes of 25 μm, and a pitch of 32 μm. The length over diameter ratio (L/D) for this collimator was 20, thus the collimator was 500 μm in length. All experiments have been performed in TOT mode. For all experiments the fitted parameter C from equations 3.2 and 3.3, is given in all figures by the parameter σ in the legend.

In order to study the spatial resolution we chose to perform the experiments with either a microscope slide or a thin copper plate. These materials are thick enough to absorb alpha particles. If these objects are placed on the chip we expect that these materials absorb all alpha particles. By counting the number of alpha particles in small bins defined from the edges of the alpha absorbing materials the spatial resolution can then be determined by plotting a step function to the binned data.

Results of the first experiment of this project are given in figure 4.8. As proposed by equation 3.3 the spatial resolution obtained in this experiment is 32.1 μm. These results showed the ability of the Timepix chip to obtain a sub-pixel spatial resolution.

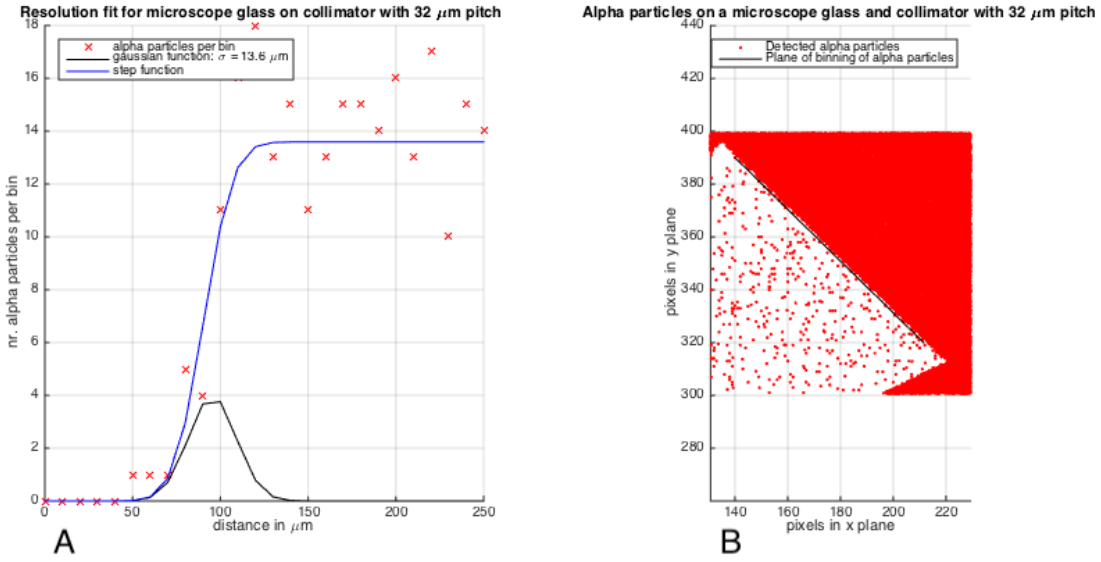

Figure 4.8: Results of experiment performed with a 32 μm collimator on a microscope glass. Figure A shows the results for fit of the step function, from which the resolution can be determined. Figure B shows the output of the Timepix for the experiment with the microscope slide. Some alpha particles did manage to surpass the thin microscope slide as figure B shows single alpha hits at the area where the microscope slide was placed. The size of binning of the alpha particles was 10 μm. Acquired spatial resolution of the Timepix chip in this experiment is 32.1 μm.

We expected that the maximum obtainable spatial resolution of a collimator is to be equal to the pitch dimensions of the collimator. The collimator used in above mentioned experiment the maximum obtainable spatial resolution is 32 μm and thus the result of the experiment is very near to this limit.

As can be seen from the image on the right hand side of figure 4.8 several alpha particles did penetrate the microscope slide. We thought that this might limit the spatial resolution so we set up a similar experiment, but instead of using the microscope slide a piece of copper plate was used. Results of this experiment are given in figure 4.9. The spatial resolution obtained from this experiment is 55.9 μm. The obtained spatial resolution with the copper experiments was not as good as the experiments performed with the microscope slide. The copper plate was cut in order to fit on the chip. We believe that the cutting of the copper plate is the limiting factor in this experiment as the experiment with the microscope slide had better performance.

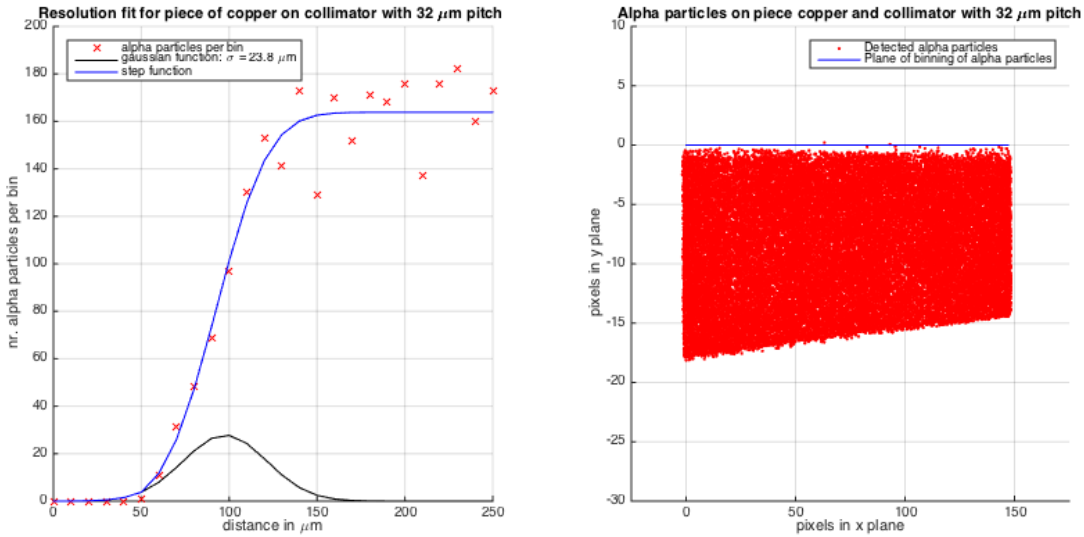

Figure 4.9: Results of experiment performed with a 32 μm collimator on a copper plate. The results show a worse spatial resolution compared to the microscope slide (55.9 and 32.1 μm respectively), most possibly due to cutting of the copper plate. The binning size for this experiment was chosen at 10 μm, which showed to be small enough as the Gaussian function is smooth.

Due to the success of the results of the experiments with the 32 μm collimator, other collimators with smaller pitch or better L/D ratio were purchased. Experiments have been performed with a collimator of 32 μm pitch, diameter 25 μm and L/D of 40. The spatial resolution acquired in this experiment is 31.5 μm, which is similar to the experiments performed with previous collimator of 32 μm but with L/D of 20. The fitted data is given in figure 4.10.

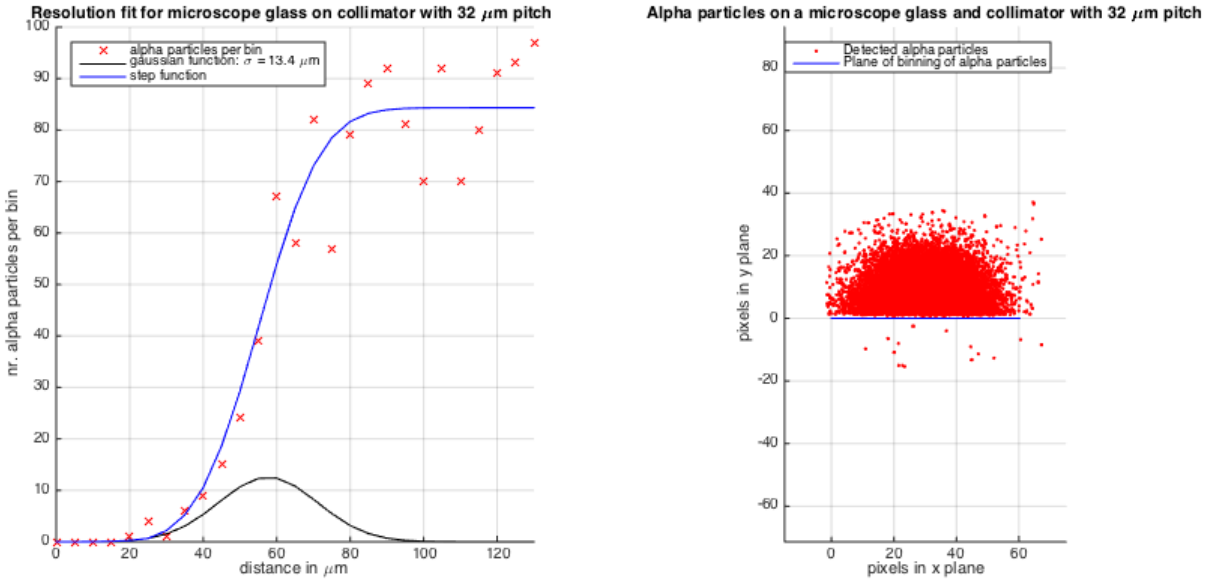

Figure 4.10: Results of experiment performed with a 32 μm collimator (40 L/D) on a microscope slide. The acquired spatial resolution is better than the expected maximum spatial resolution (31.5 and 32.1 μm respectively).

The fitted data and a plot of the detected alpha particles with a collimator of 12 μm pitch is given in figure 4.11. The acquired spatial resolution in this plot is 14.5 μm.

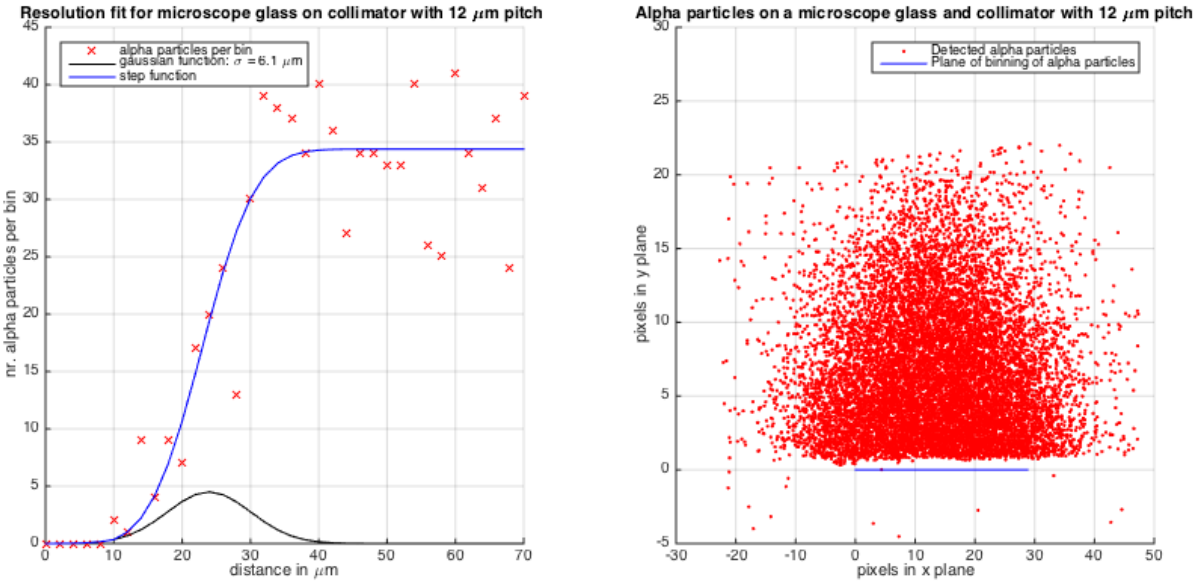

Figure 4.11: Results for experiments with 12 μm pitch collimator. Binning size for this experiment was 2 μm. Spatial resolution of Timepix chip in this experiment is 14.5 μm.

Results for the finest used collimator are given in figure 4.12. The collimator has a pitch of 6 μm. Obtained spatial resolution from this experiment is 9.8 μm which is substantially better then the results obtained with collimator of 12 μm pitch. These results do tend to show however, that a spatial resolution of around 10 μm is the maximum feasible spatial resolution of the Timepix chip. The obtained spatial resolution is significantly larger then the size of the pitch, this did not apply to the previous experiments as the obtained resolution was of order of size of the pitch. These experiments showed that sub-pixel spatial resolution in alpha particle imaging on a Timepix chip is possible. The use of the TOT mode in these experiments improved location reconstruction from interaction of alpha particles with the silicon sensor.

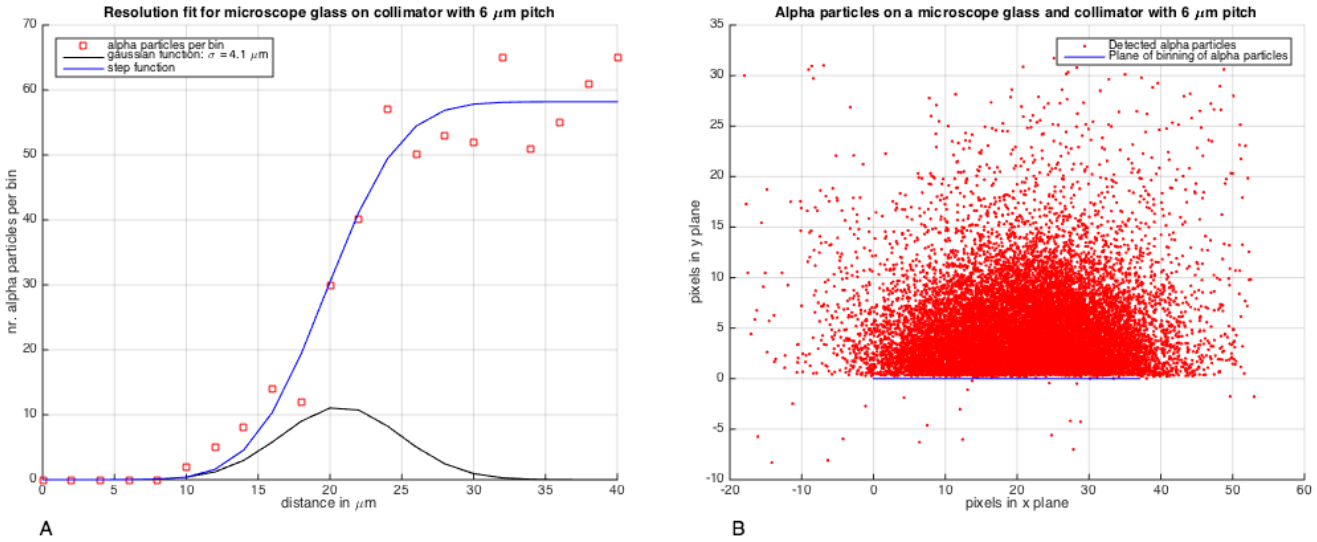

Figure 4.12: Results for experiments with finest collimator (pitch of 6 μm). Binning size for this experiment was 2 μm. Spatial resolution of Timepix chip for this experiment is 9.8 μm.

4.4. Energy Resolution Measurements

The experimental method for the energy resolution measurements has been described in section 3.1. Before the results will be given and discussed the argumentation of the approach of the experimental method will be discussed.

The time over threshold (TOT) mode of the Timepix chip was selected in the experiments. As discussed the TOT mode's output is a measure of the interacting particle energy. The output of an alpha particle in TOT mode on the Timepix chip has been given in figure 3.5B, the integrated volume of such a 'blob' is the alpha particles energy. In these experiments we measured alpha particles with different energies, where we expected that by means of the TOT mode we could identify and separate the observed alpha particles based on their energy. The four chips of the Timepix device can be influenced by several parameters, but the most important parameter is the THL value. The THL value, or the Fine Lower Threshold, is a set voltage that controls the energy discrimination threshold in pixels. For each chip a THL level is set. The Timepix chip is operated in positive polarity, which means that for lower values of the threshold level the higher the energy discrimination level. Due to tolerances in the manufacturing process the output of the chips are not similar for even THL levels. The chips must thus be calibrated before start of the energy resolution measurements.

The calibration of the Timepix chip was performed by the following experiments. In these experiments the Am-241 source was placed in front of the Timepix chip. For all 4 chips the THL value was changed in order to equalize the blob size. The results for the mean volume and mean pixels in a cluster is given in figure 4.13. For each chip the THL level was set such that the mean volume of an alpha particle was 400. The experiments were performed in a 3D printer collimator holder, which is given in figure A.1 in the Appendix. From the results we observe that chip 1 has a relatively low THL value for mean volume of 400, while the other chips are more alike. The mean pixel size of alpha particles for these THL levels has been plotted for all chips. Remarkable is that the mean pixel size for chip 1 is significantly lower than other chips.

Equalization of volume of (same energy) alpha particles on the four chips by means of the THL value is rather difficult. In the experiments the Americium-241 source had to be moved to the correct spot above the corresponding chip. In these experiments it is likely that the distance towards the interface of the chip was not similar for all experiments for the four chips, but small deviations due to the placement of the source is possible. Such small deviations are not much larger than 1 millimeter but from other experiments we have seen that this has a significant influence on the outcome of the mean volume. The used collimator in these experiments was glued to the 3D printed collimator holder. In this operation some glue got spilled over the edges of the collimator. This can be seen from figure 4.14, results show that the interface of chip 0 was clean. Because of the deviations in the placement of the source on the corresponding chip and the fact that on some edges glue was spilled we chose to focus on chip 0 for the energy resolution measurements.

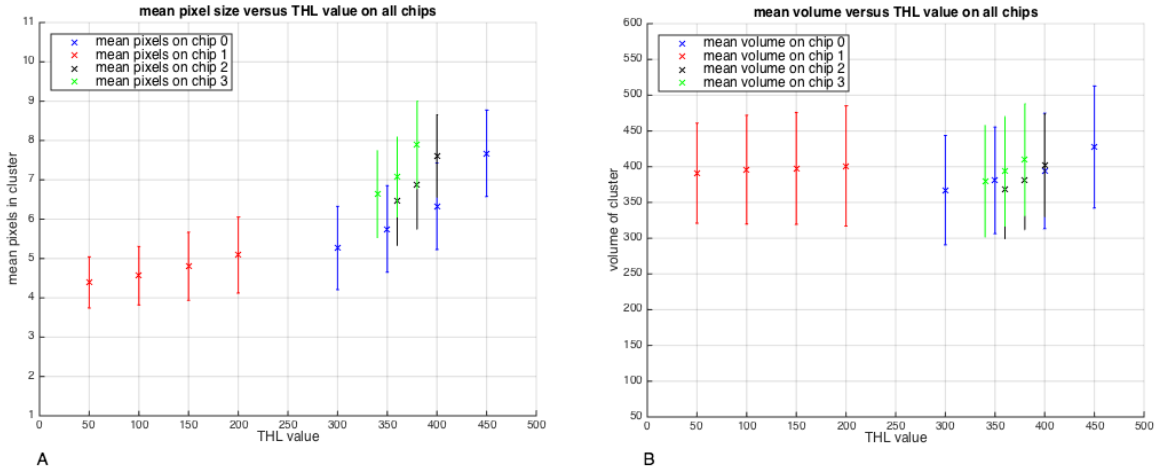

Figure 4.13: Results for variation of THL levels on mean particle size (fig A) and mean cluster volume (fig B) for of imaging 5.5 MeV alpha particle on Timepix chips. In order to perform energy measurements on the whole Timepix device (all 4 chips) equalization of the cluster volume for the chips is necessary to obtain similar output.

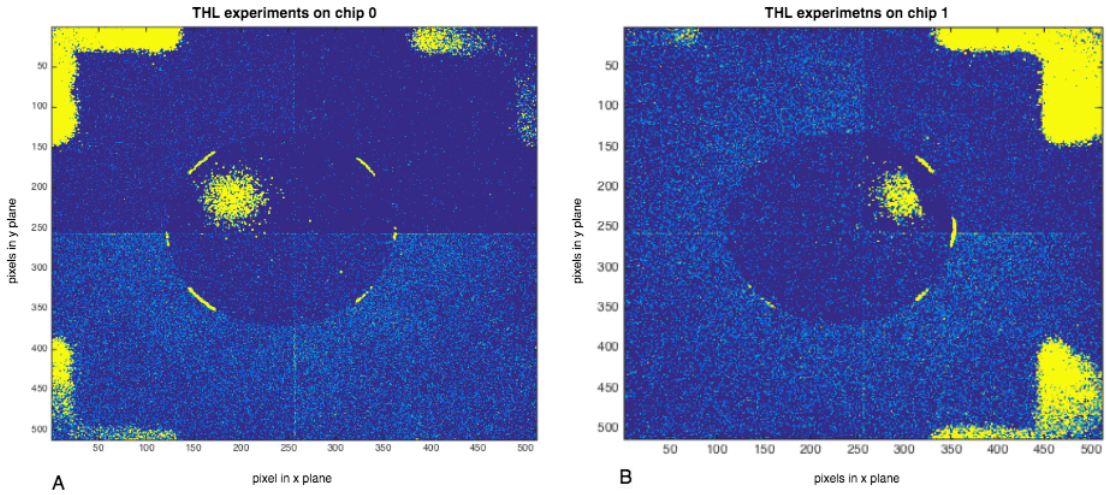

Figure 4.14: Results on Timepix chip after irradiating with Americium-241 in smoke detector on chip 0 (figure A) and chip 1 (figure B). The smoke detector was placed just above the collimator holder, the contours of this collimator holder can clearly be seen from this figure. In both figures we see the collimator as a perfect circle, and the shape of the Am-241 source as a tiny irradiated circle on the figures. For figure B this is not a complete circle, but part of it has been withheld from the image. This edge is due to some excess glue that was used to mount this collimator. Chip 0 is the northwestern square, chip 1 northeast, chip 2 southeast, and chip 3 southwest.

Now that chip 0 was chosen to perform the energy measurements we wanted to study the response of the Timepix chip to alpha particles of various energies. We used a similar experimental set-up used in the previous experiments with the output equalization of the four chips. The collimator holder figured in the Appendix in figure A.1 was used, the Americium-241 smoke detector was placed right above the sample holder. Alpha particles of various energies were obtained by slowing them down with several layers of Mylar foil. The Mylar foils were placed between the collimator holder and the Timepix chip. The experiments were performed for THL levels of 300 and 350. Results of these experiments are given in figure 4.15.

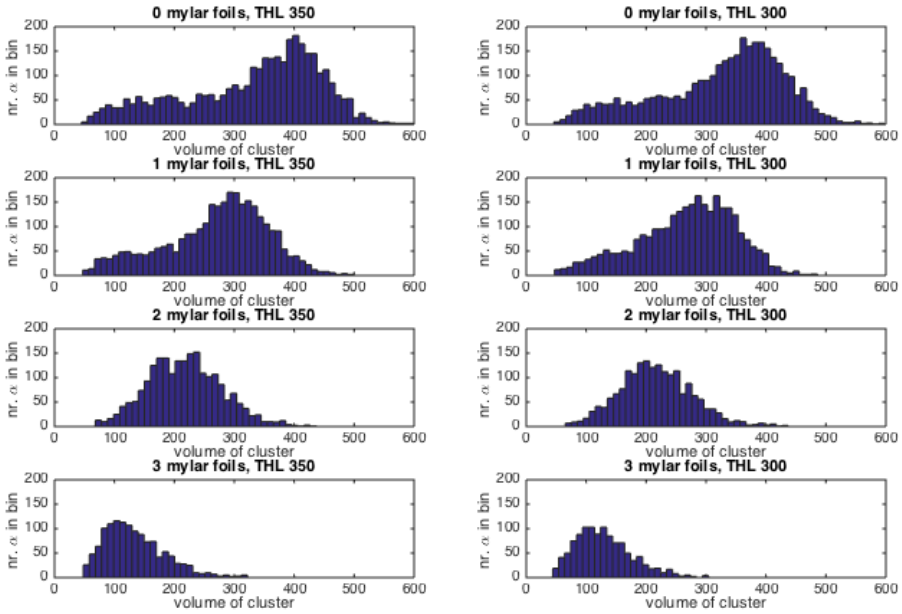

Figure 4.15: Results for imaging alpha particles slowed down by Mylar foil for THL 350 (figure A) and THL 300 (figure B). The influence of THL value is slightly visible as the data for THL 350 has higher mean volume of cluster events. The influence of the Mylar foils is clearly visible as both the total number of alpha particles that are transmitted is decreased as the mean total energy of the alpha particles is decreased for increasing number of Mylar foils. Calculation of the energy of the alpha particles has not been performed for these measurements but has been for the final measurements of the energy resolution measurements.

The results given in figure 4.15 clearly show a relation between the volume of the alpha particle's cluster and its incidental energy. The expected signal of a monochromatic alpha-emitting source would be a perfect Dirac delta function, thus a narrow spike at some value for volume of clusters. The results show however, that the observed alpha particle energy is not monochromatic as for a singular measurement a range of volume clusters is measured. We can see that the signal for 0 Mylar foils builds up to a Gaussian like shape, after which the signal dies out. We consider the maximum of this Gaussian to be the measured alpha particle energy. We believe that the build up of these charges is due to impurities in the charge collection process. Either because of impurities in the silicon, or due to recombination of the charge carriers.

The results of figure 4.15 show as expected that the total summed alpha particle energy decreases for increasing Mylar thickness, and thus for decreasing alpha particle energy. The alpha particle energy needs to be calculated in order to conclude anything about possible energy resolution limits. Moreover, the Mylar foils were placed at the end of the trajectory of an alpha particle, just before interacting with sensor material. In this part of its trajectory the alpha particle might loose a lot of energy per unit length due to the fact that the alpha particle is at the rather end of the Bragg spectrum. In order to have smaller intervals of decreasing alpha particle energy it is more useful if the Mylar foils are placed at the start of the trajectory of the particle.

For the final energy resolution measurements the Mylar foils are placed at the beginning of its trajectory to the Timepix chip. All measurements were performed on chip 0 of the Timepix device. A schematic representation of this set-up is given in figure A.2. The results of these experiments are given in figure 4.16.

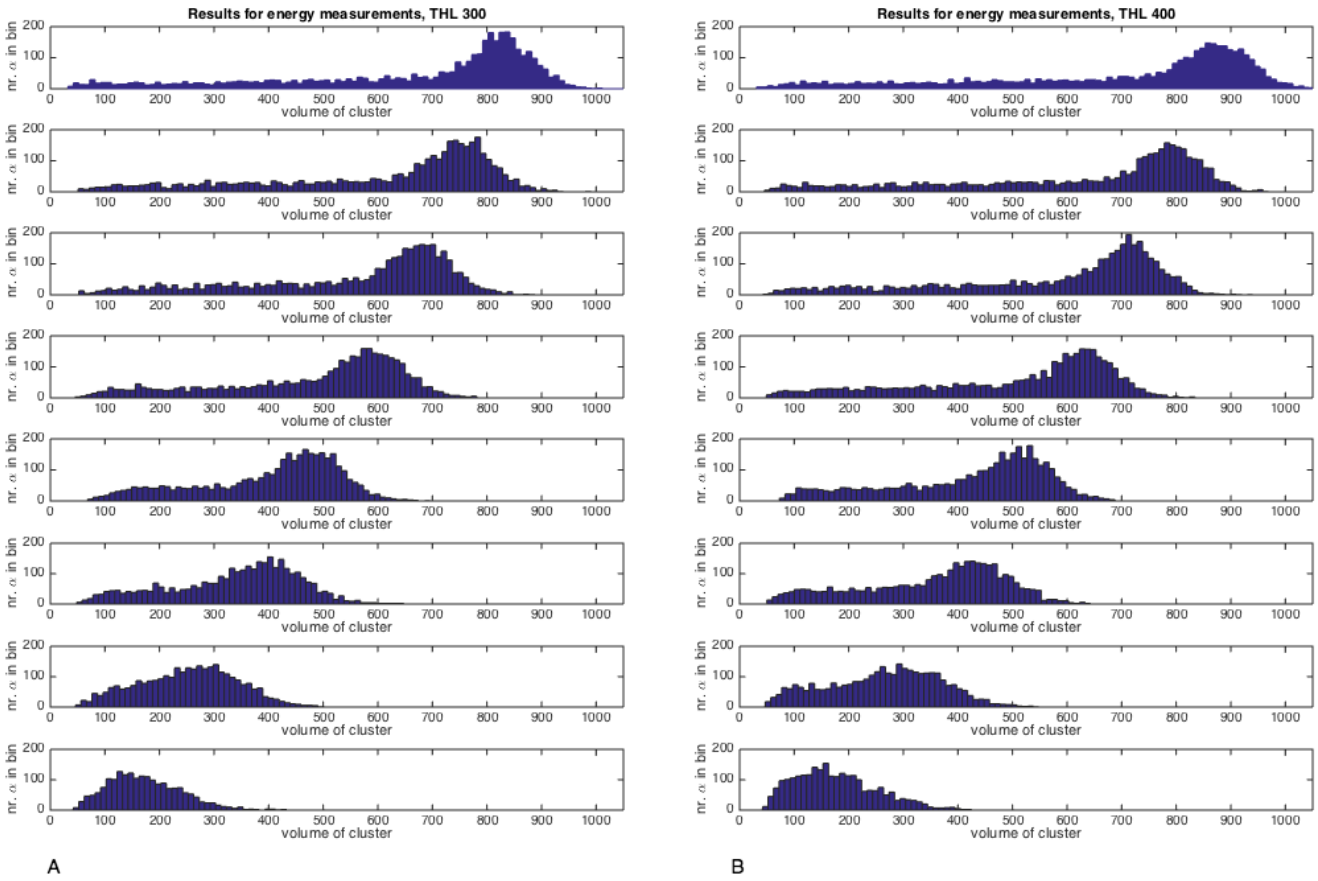

Figure 4.16: Results for Mylar measurements at THL 300 (figure A) and THL 400 (figure B). The topmost histogram for both figures is data for 0 Mylar foils, then for each histogram beneath the number of Mylar foils are gradually increased. The lowest histogram thus is data for experiment with 7 Mylar foils. A clear distinction in energy spectrum is seen as the Mylar foils are increased, but the alpha particle's energy is not yet known.

These results show a clear pattern of energy and signal loss due to an increasing number of Mylar foils. Both figures show similar data for the two THL values. Just as the experiments given in figure 4.15 the signal has a slow and steady build up, until a Gaussian shaped signal is observed. For further computations the maximum of this Gaussian shaped data is taken as the alpha particles energy. An issue for these results is that the energy of the alpha particles used in these experiments needs to be quantified. Along its trajectory to the chip the alpha particle interacts with air, Mylar foils, some more air, aluminum after which is finally interacts and ionizes silicon. The energy loss of the alpha particle along its trajectory needs to be calculated such that the energy of the alpha particle upon interacting with the chip is known.

The American National Institute of Standards and Technology (NIST) offers free available databases for the stopping power and range of electrons, protons and helium ions (alpha particles) in several specified materials [45]. In this database the stopping power (S) is given in MeV cm^2/g for alpha particles of energy up to GeV's. Multiplying S by the material density one obtains the energy loss per unit length, from which the Bragg curves for any specified energetic alpha particles are obtained. The alpha particles energy loss can be calculated by integrating the Bragg curve from x = 0 to the covered distance by the alpha particle. Computations have been performed in order to calculate the energy loss of alpha particles along the trajectory given in figure A.2. Results of the calculated energies of alpha particles along this trajectory are given in figures 4.17 and 4.18. As can be seen from the figures the alpha particles lose quite some of their kinetic energy as a result of interactions with air, Mylar, aluminum and silicon. The results in the legend of figure 4.18 give the final energies of the alpha particles after their trajectory.

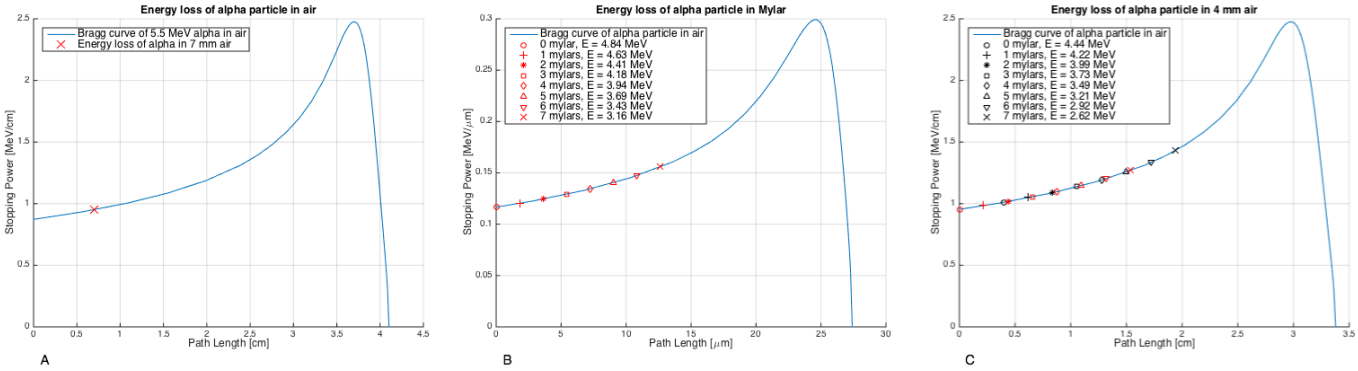

Figure 4.17: Fitted Bragg curves for trajectory of alpha particle in 7 millimeters of air (figure A), Mylar foils (figure B), and 4 millimeters of air (figure C). The energies after traversing the materials (air or Mylar) are given in the legend for all figures. At the beginning of the trajectory of an alpha particle in the energy experiments the incidental energy is 5.5 MeV, after which some energy is lost due to traversing 7 millimeters of air. Figure B shows the fitted results for the energy loss of an alpha particle in several layers of Mylar foil. For example, after 7 millimeters of air and 3 layers of Mylar foil the alpha only has an energy of 4.18 MeV. Figure C shows the shift in energy loss when the alpha particles traverse 4 more millimeters in air, denoted by the black symbols in the figure.

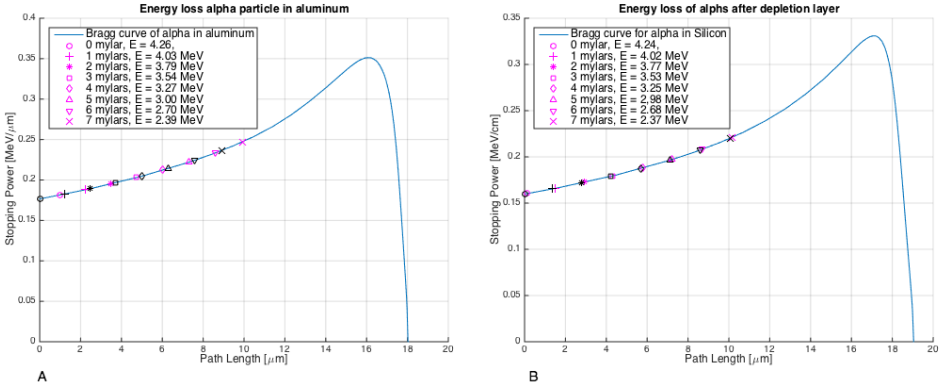

Figure 4.18: Fitted results for alpha particle traversing aluminum (figure A) and depletion layer (figure B). Final energies of alpha particle at end of its trajectory are given in the legend of figure B. By these calculations, this are the energies that are detected by the Timepix chip.

As the energies of the alpha particles at points at their trajectories are calculated it is possible to identify the total detected charge by the Timepix chip for the 0 to 7 Mylar foils. Results for both values of THL for experiments with 0 to 2 Mylar foils, as well as a Gaussian fit is given in figure 4.19. The FWHM of the fitted Gaussian function is a measure of energy resolution of the system. In the legend of the results the FWHM has been given for all 6 experiments. Results of these experiments show that the energy resolution is in order of 0.8 MeV.

An energy resolution in order of 0.8 MeV of the Timepix chip allows for (some of) the identification of daughter radionuclides in the decay of Ac-225 (figure 2.4). However, the decay of Fr-221 (6.46 MeV) is hard to distinguish from decay from Ac-225 (5.94 MeV). If a sample is obtained that can be measured for a significant period of time then a relevant study can be made to the accumulation of daughter radionuclides of Ac-225. If enough alpha particles interact with the silicon sensor then it is expected that Gaussian curves arise for the relevant energies of the daughter radionuclides. For single alpha particles it is however very difficult to determine the parent radionuclide as the response of the Timepix chip has a very broad energy spectrum, as can be seen in all (histogram) results. Therefore long measurement times are necessary to ensure reliable data.

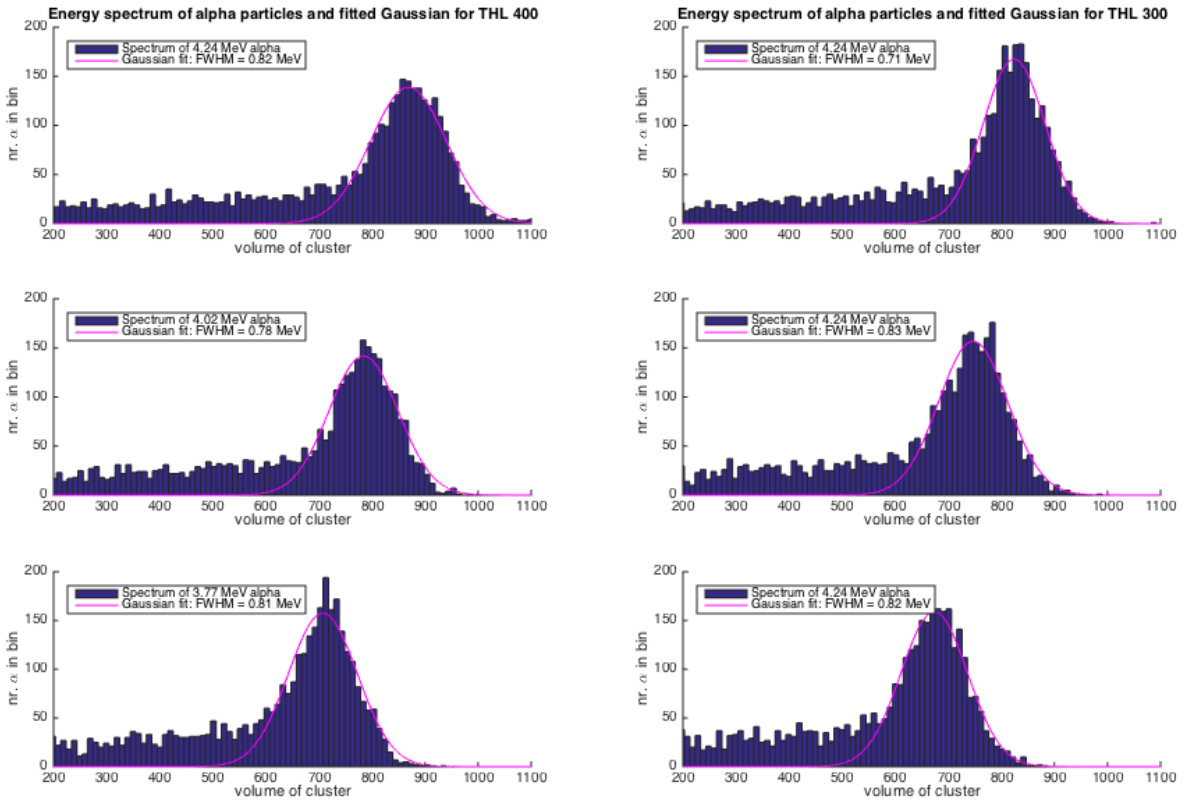

Figure 4.19: Obtained results for energy spectrum of alpha particles + the fitted Gaussian functions for THL 400 (figure A), and THL 300 (figure B). The fit for the Gaussian functions has only been selected on a certain interval of the histogram data, as the 'build-up' in these histograms is due to inefficiencies in the charge collection of the Timepix chip. The FWHM is an indication for the (energy) resolution of the chip. The FWHM value has been given in the legend for both THL values and 0 to 2 Mylar foils.

5

Conclusion & Recommendations

5.1. Conclusion

Imaging alpha radiation in biological samples is challenging because of the short range of kinetic alpha particles. The classic alpha camera is an existing alpha imaging technique which is based on a scintillating layer that absorbs alpha particles and emits photons. The system can acquire a spatial resolution up to 35 μm but the system is limited by the absorption of x-rays, photons and beta particles of the scintillating layer. Another imaging method for alpha radiation is a Timepix device. Timepix is a hybrid pixelated semiconducting sensor that consists of an array of 55 μm square pixels. This work studied the response of a Timepix chip to alpha irradiation and sought for the limits of the device regarding spatial and energy resolution. An overall conclusion of this research is given below, as well as recommendations for future research is given.

The first part of the research focused on the calibration of an alpha-emitting source. The source, a 3.7 MBq Americium-241, is owned by the Erasmus MC and is used with a collimator for dosimetry purposes. The activity of the source in a collimator was unknown so a study with the Timepix has been made. Results showed that the total activity at 2.5 millimeters was 82 KBq. After this project was finished the focus shifted to imaging alpha particles from the decay of Actinium-225. Samples treated with the alpha emitter were obtained in order to study the accumulation of Actinium-225 in the sample, which was expected to accumulate at the edges of cultured spheroids. The activity in the samples was in the order of a few Bq so long exposure times were necessary. Results showed that the Timepix device does respond to low activity, but for determination of accumulation of the Actinium-225 we learned that the use of a collimator is essential in to ensure a monochromatic particle beam.

Results for the spatial resolution measurements showed that the use of a fine collimator can ensure a subpixel resolution. A spatial resolution of 14.5 μm was obtained by using a collimator with pitch of 12 μm, and a spatial resolution of 9.8 μm is obtained with a collimator with pitch of 6 μm. The use of a collimator with finer pitch than 6 μm is not expected to improve the spatial resolution as the obtained resolution is significantly bigger than the dimensions of the pitch of the used collimator.

The energy resolution to imaging kinetic alpha particles via the Timepix chip was determined at 0.8 MeV. Experiments were performed by slowing down alpha particles via Mylar foil and observing the energy spectrum. Results showed that the energy spectrum is rather broad, possible due to impurities in the silicon sensor material or due to recombination of charge carriers. The energy resolution was obtained by fitting a Gaussian function to the obtained energy spectrum. The 0.8 MeV energy resolution allows for the identification of most daughter nuclides in the decay of Ac-225. The decay of Fr-221 (6.46 MeV) is however hard to distinguish from the decay of Ac-225 (5.94 MeV) by the Timepix chip.

5.2. Recommendations

Results for the spatial resolution are very promising for TAT applications as the obtained spatial resolution is almost similar to cellular dimensions. The use of a very well defined edge of an object (order of 5 μm, via laser cutting for example) would be a great experiment to study the influence of the edge of the microscope glass on the spatial resolution of the Timepix.

Results for the energy resolution spectrum showed that the Timepix chip is able to identify and isolate the daughter radionuclides of Actinium-225. However the obtained energy spectrum from these experiments show that the spectrum is rather broad for a well-known energy of an alpha particle. Due to tolerances in the production of the pixels the output of the chips is not similar. Not only does the system need a calibration for the chips, but especially a pixel-to-pixel calibration is needed such that the TOT value of a single pixel cell can be weighted for the particles energy. This is a time consuming process but can improve the energy resolution of the Timepix system significantly.

A

Appendix

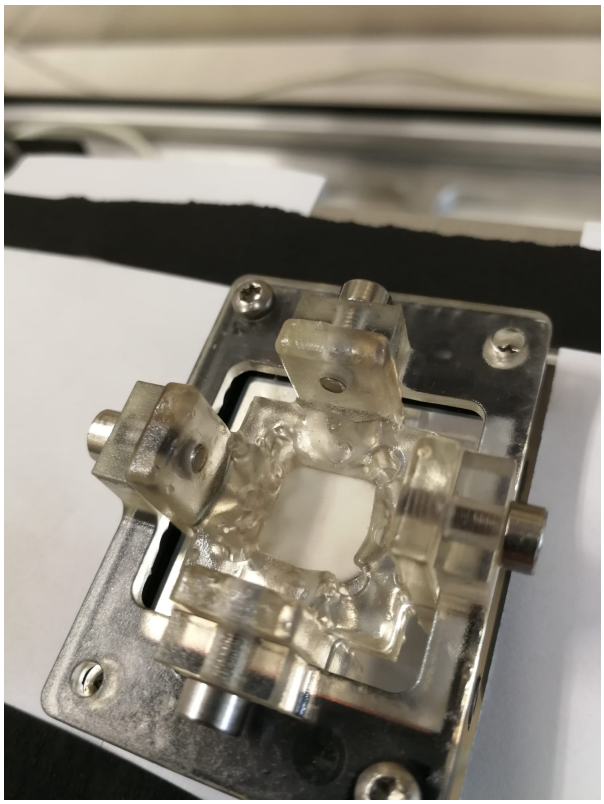

Figure A.1: Image of the 3D printer collimator holder. By use of this holder it was possible to place the collimator at only a fraction of a millimeter above the sensor material.

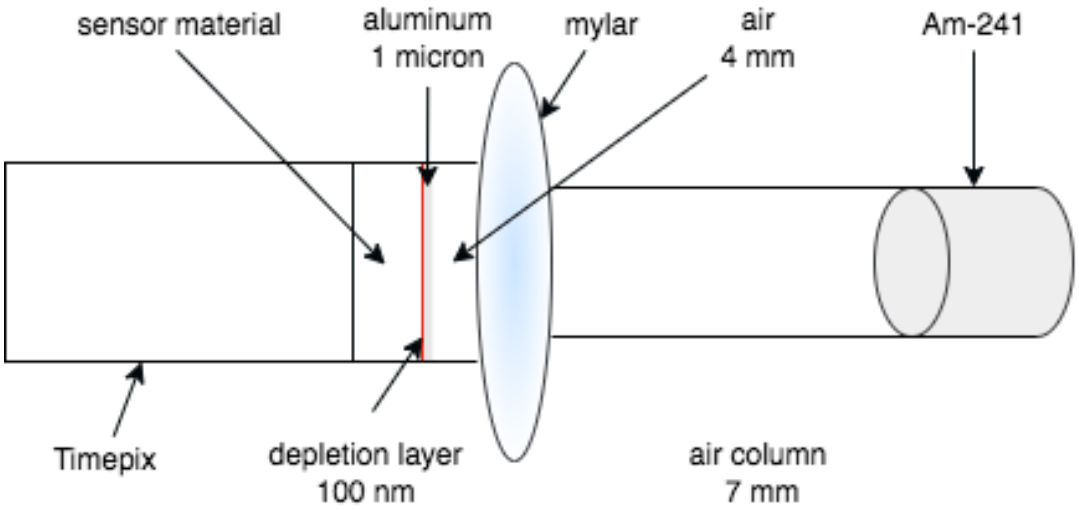

Figure A.2: Schematic representation of the set-up used in the final energy measurements. Once emitted the alpha particles first traverse 7 millimeters of air before surpassing the Mylar foils, after which another 4 millimeters of air need to be crossed. The surface of the Timepix chip is coated with 1 μm of aluminum. Because of diffusion effects of the created charge carriers in the silicon material a depletion layer is formed, where charges can not be collected at pixel bonds. By means of an educated guess the thickness of depletion layer has been said to be 100 nanometers.

Bibliography

[1] A. R. Rao, V. Hanchanale, M. Laniado, O. Karim, and H. Motiwala, "Sir percival pott and his memorable contribution to the epidemiology of the chimney sweeper's cancer and the epidemic of tuberculosis", The Journal of Urology **179**, 310–310 (2008).

[2] J. Ferlay, M. Ervik, F. Lam, M. Colombet, L. Mery, M. Piñeros, A. Znaor, I. Soerjomataram, and F. Bray, Global cancer observatory: cancer today. lyon: international agency for research on cancer; 2018, 2020.

[3] F. D. Guerra Liberal, J. M. O'Sullivan, S. J. McMahon, and K. M. Prise, "Targeted alpha therapy: current clinical applications", Cancer biotherapy & radiopharmaceuticals **35**, 404–417 (2020).

[4] C. Parker, S. Nilsson, D. Heinrich, S. I. Helle, J. O'sullivan, S. D. Fosså, A. Chodacki, P. Wiechno, J. Logue, M. Seke, et al., "Alpha emitter radium-223 and survival in metastatic prostate cancer", New England Journal of Medicine **369**, 213–223 (2013).

[5] R. M. De Kruijff, H. T. Wolterbeek, and A. G. Denkova, "A critical review of alpha radionuclide therapy—how to deal with recoiling daughters?", Pharmaceuticals **8**, 321–336 (2015).

[6] G. Sgouros, "Alpha-particles for targeted therapy", Advanced drug delivery reviews **60**, 1402–1406 (2008).

[7] T. Bäck and L. Jacobsson, "The α-camera: a quantitative digital autoradiography technique using a charge-coupled device for ex vivo high-resolution bioimaging of α-particles", Journal of Nuclear Medicine **51**, 1616–1623 (2010).

[8] X. Llopart, R. Ballabriga, M. Campbell, L. Tlustos, and W. Wong, "Timepix, a 65k programmable pixel readout chip for arrival time, energy and/or photon counting measurements", Nuclear Instruments and Methods in Physics Research Section A: Accelerators, Spectrometers, Detectors and Associated Equipment **581**, 485–494 (2007).

[9] A. Rosenfeld, S. Alnaghy, M. Petasecca, D. Cutajar, M. Lerch, S. Pospisil, V. Giacometti, R. Schulte, V. Rosso, M. Würl, et al., "Medipix detectors in radiation therapy for advanced quality-assurance", Radiation Measurements **130**, 106211 (2020).

[10] J. Jakubek, "Precise energy calibration of pixel detector working in time-over-threshold mode", Nuclear Instruments and Methods in Physics Research Section A: Accelerators, Spectrometers, Detectors and Associated Equipment **633**, S262–S266 (2011).

[11] R. AL Darwish, A. H. Staudacher, E. Bezak, and M. P. Brown, "Autoradiography imaging in targeted alpha therapy with timepix detector", Computational and mathematical methods in medicine **2015** (2015).

[12] R. Al Darwish, A. Staudacher, Y. Li, M. Brown, and E. Bezak, "Development of a transmission alpha particle dosimetry technique using a549 cells and a ra-223 source for targeted alpha therapy", Medical physics **43**, 6145–6153 (2016).

[13] J. Valentin, "Relative biological effectiveness (rbe), quality factor (q), and radiation weighting factor (wr): icrp publication 92", Annals of the ICRP **33**, 1–121 (2003).

[14] E. Gazis, "The ionizing radiation interaction with matter, the x-ray computed tomography imaging, the nuclear medicine spect, pet and pet-ct tomography imaging", Medical Imaging: Principles and Applications, 41 (2019).

[15] J. E. Parks, "Attenuation of radiation", Department of Physics and Astronomy The University of Tennessee, Tennessee (2001).

[16] A. B. Chilton, J. K. Shultis, and R. E. Faw, "Principles of radiation shielding", (1984).

[17] Y.-S. Kim and M. W. Brechbiel, "An overview of targeted alpha therapy", Tumor biology **33**, 573–590 (2012).

[18] M. R. Zalutsky and D. D. Bigner, "Radioimmunotherapy with α-particle emitting radioimmunoconjugates", Acta Oncologica **35**, 373–379 (1996).

[19]T. K. Nikula, M. R. McDevitt, R. D. Finn, C. Wu, R. W. Kozak, K. Garmestani, M. Brechbiel, M. J. Curcio, C. G. Pippin, L. Tiffany-Jones, et al., "Alpha-emitting bismuth cyclohexylbenzyl dtpa constructs of recombinant humanized anti-cd33 antibodies: pharmacokinetics, bioactivity, toxicity and chemistry", Journal of Nuclear Medicine **40**, 166–176 (1999).

[20]J. Elgqvist, S. Frost, J.-P. Pouget, and P. Albertsson, "The potential and hurdles of targeted alpha therapy–clinical trials and beyond", Frontiers in oncology **3**, 324 (2014).

[21]M. G. Ferrier and V. Radchenko, "An appendix of radionuclides used in targeted alpha therapy", Journal of medical imaging and radiation sciences **50**, S58–S65 (2019).

[22]M. R. McDevitt, G. Sgouros, and S. Sofou, "Targeted and nontargeted α-particle therapies", Annual review of biomedical engineering **20**, 73–93 (2018).

[23]M. R Zalutsky and M. Pruszynski, "Astatine-211: production and availability", Current radiopharmaceuticals **4**, 177–185 (2011).

[24]S. Lindegren, P. Albertsson, T. Bäck, H. Jensen, S. Palm, and E. Aneheim, "Realizing clinical trials with astatine-211: the chemistry infrastructure", Cancer biotherapy & radiopharmaceuticals **35**, 425–436 (2020).

[25]T. L. Rosenblat, M. R. McDevitt, D. A. Mulford, N. Pandit-Taskar, C. R. Divgi, K. S. Panageas, M. L. Heaney, S. Chanel, A. Morgenstern, G. Sgouros, et al., "Sequential cytarabine and α-particle immunotherapy with bismuth-213–lintuzumab (hum195) for acute myeloid leukemia", Clinical cancer research **16**, 5303–5311 (2010).

[26]A. K. Robertson, C. F. Ramogida, C. Rodriguez-Rodriguez, S. Blinder, P. Kunz, V. Sossi, and P. Schaffer, "Multi-isotope spect imaging of the 225ac decay chain: feasibility studies", Physics in Medicine & Biology **62**, 4406 (2017).

[27]M. Miederer, D. A. Scheinberg, and M. R. McDevitt, "Realizing the potential of the actinium-225 radionuclide generator in targeted alpha particle therapy applications", Advanced drug delivery reviews **60**, 1371–1382 (2008).

[28]F. Lacoeuille, N. Arlicot, and A. Faivre-Chauvet, "Targeted alpha and beta radiotherapy: an overview of radiopharmaceutical and clinical aspects", Médecine Nucléaire **42**, 32–44 (2018).

[29]X. Llopart Cudié, "Design and characterization of 64k pixels chips working in single photon processing mode", PhD thesis (Mid Sweden Unv, 2007).

[30]L. Abate, E. Bertolucci, M. Conti, A. Di Cosmo, C. Di Cristo, G. Mettivier, M. Montesi, and P. Russo, "Quantitative dynamic imaging of biological processes with solid state radiation detector", IEEE Transactions on Nuclear Science **47**, 1907–1910 (2000).

[31]S. Gohl, B. Bergmann, H. Evans, P. Nieminen, A. Owens, and S. Posipsil, "Study of the radiation fields in leo with the space application of timepix radiation monitor (satram)", Advances in Space Research **63**, 1646–1660 (2019).

[32]J. Zemlicka, J. Jakubek, M. Kroupa, D. Hradil, J. Hradilova, and H. Mislerova, "Analysis of painted arts by energy sensitive radiographic techniques with the pixel detector timepix", Journal of Instrumentation **6**, C01066 (2011).

[33]P. Kostamo, S. Nenonen, S. Vähänen, L. Tlustos, C. Fröjdh, M. Campbell, Y. Zhilyaev, and H. Lipsanen, "Gaas medipix2 hybrid pixel detector", Nuclear Instruments and Methods in Physics Research Section A: Accelerators, Spectrometers, Detectors and Associated Equipment **591**, 174–177 (2008).

[34]C. Fröjdh, H. Graafsma, H. Nilsson, and C. Ponchut, "Characterization of a pixellated cdte detector with single-photon processing readout", Nuclear Instruments and Methods in Physics Research Section A: Accelerators, Spectrometers, Detectors and Associated Equipment **563**, 128–132 (2006).

[35]E. J. Schioppa, "The color of x-rays", Nikhef Amsterdam (2014).

[36]C. Jiang, S. J. Moniz, A. Wang, T. Zhang, and J. Tang, "Photoelectrochemical devices for solar water splitting–materials and challenges", Chemical Society Reviews **46**, 4645–4660 (2017).

[37]M. Rizzi, M. D'Aloia, and B. Castagnolo, "Semiconductor detectors and principles of radiation-matter interaction", Journal of Applied Sciences(Faisalabad) **10**, 3141–3155 (2010).

[38]P. Tsopelas, "A silicon pixel detector for lhcb", PhD thesis (Vrije U., 2016).

[39]H. Spieler, Semiconductor detector systems, Vol. 12 (Oxford university press, 2005).

[40] P. Wexler, B. D. Anderson, S. C. Gad, P. B. Hakkinen, M. Kamrin, A. De Peyster, B. Locey, C. Pope, H. M. Mehendale, and L. R. Shugart, Encyclopedia of toxicology, Vol. 1 (Academic Press, 2005).

[41] M. Hoheisel, A. Korn, and J. Giersch, "Influence of backscattering on the spatial resolution of semiconductor x-ray detectors", Nuclear Instruments and Methods in Physics Research Section A: Accelerators, Spectrometers, Detectors and Associated Equipment **546**, 252–257 (2005).

[42] J. Poston, "Dosimetry", in Encyclopedia of physical science and technology (third edition), edited by R. A. Meyers, Third Edition (Academic Press, New York, 2003), pp. 603–650.

[43] MATLAB, Version 8.4.0 (r2014b) (The MathWorks Inc., Natick, Massachusetts, 2014).

[44] G. Audi, F. Kondev, M. Wang, W. Huang, and S. Naimi, "The nubase2016 evaluation of nuclear properties", Chin. Phys. C **41**, 030001 (2017).

[45] R. Walters, "Stopping-power & range tables for electrons, protons, and helium ions", NIST Standard Reference Database 124, NIST (2017).